High sensitivity lithium fluoride as a detector for environmental dosimetry

Davis, Stephen D.

Report (National Research Council of Canada. Institute for National Measurement Standards. Ionizing Radiation Standards); no. PIRS-0832, 2003-01

High Sensitivity Lithium Fluoride As a Detector for Environmental Dosimetry (M.Sc. Thesis)

S. D. Davis

January, 2003

PIRS-0832

Ionizing Radiation Standards
Institute for National Measurement Standards
National Research Council
Ottawa, Ontario, K1A 0R6

Telephone: 613-993-2197
Fax: 613-952-9865
E-mail: carl.ross@nrc.ca

HIGH SENSITIVITY LITHIUM FLUORIDE

AS A DETECTOR FOR ENVIRONMENTAL DOSIMETRY

by

STEPHEN D. DAVIS, B.Sc.

Medical Physics Unit

McGill University, Montreal

January 2003

A thesis submitted to McGill University

in partial fulfilment of

the requirements for the degree of

Master of Science

Abstract

A new thermoluminescence dosimetry system for environmental applications was tested, which used high sensitivity lithium fluoride (TLD-100H). The energy response of the bare thermoluminescence dosimeters (TLDs) was measured for photon beams with mean energies from 24 keV to 1.1 MeV, and the results were compared with standard lithium fluoride (TLD-100). The energy response was also measured for TLD-100H card-mounted dosimeters encapsulated in Teflon®, used as part of the Harshaw Type 8855 environmental dosimeter. The EGSnrc Monte Carlo system was used to calculate the dose to the TLDs in both the bare chip holder and the 8855 dosimeter, in order to calculate the thermoluminescence per unit of absorbed dose to the TLDs. The results were broadly consistent with existing data, with the response of both TLD materials correlating with the ionization density of the photon beams.

Résumé

Un nouveau système de dosimétrie par thermoluminescence pour les applications environementales, utilisant du fluorure de lithium à haute sensitivité (TLD-100H), fut évalué. La réponse énergétique du dispositif thermoluminescent (DTL) fut mesurée pour des faisceaux de photons d'énergie moyenne entre 24 keV et 1.1 MeV, et les résultats furent comparés au fluorure de lithium conventionel (TLD-100). La réponse énergétique fut également mesurée pour des dispositifs TLD-100H encapsulés de Teflon®, faisant partie du dosimètre environemental Harshaw Type 8855. Le système de Monte Carlo EGSnrc fut utilisé pour estimer la dose fournie aux DTL dans le support simple ainsi qu'intégrés au dosimètre 8855, dans le but de calculer la thermoluminescence par unité de dose absorbée par le DTL. Les résultats furent largement en accord avec les données existantes, la réponse des deux matériaux DTL démontrant une corrélation avec la densité d'ionization des faisceaux photoniques.

Acknowledgements

I would first like to acknowledge my thesis supervisor, Dr. Carl Ross, for his invaluable assistance and direction throughout the course of my research. I would also like to acknowledge John Chase and Ontario Power Generation for the financial support and research materials necessary for the project, as well as for providing the initial incentive to pursue this area of research.

In addition I would like to thank Dr. Paul Mobit for providing the resources to run the Monte Carlo simulations, and to Dr. Jan Seuntjens and Fadi Hobeila for providing the file of updated photon cross sections.

I would also like to acknowledge all of the staff in the Ionizing Radiation Standards group at the National Research Council. Dr. Len van der Zwan and Hong Shen provided assistance with the x-ray irradiations, Stewart Walker assisted with electronics issues, David Marchington constructed most of the irradiation apparatus used in this work, and Feridoun Farahvash provided support for computing issues. Dr. Ken Shortt helped arrange the project and remained in contact from his new position in Vienna.

Finally, I would like to thank the staff at Saint-Gobain Crystals and Detectors for providing some of the data and software used in this work, and John Pyatt at Ontario Power Generation for his work on the initial stages of the project.

Contents

List of Figures

List of Tables

Chapter 1

Introduction

Environmental dosimetry is the process of assessing radiation doses to members of the public around nuclear and radiological facilities (Klemic *et al* 1999). Environmental dosimetry programs can cover external and internal radiation exposures, and are normally required for the facility to demonstrate compliance with national regulations on dose limits to the public. Environmental dosimeters used for external radiations are generally used to measure the doses received from γ-rays or x-rays, and can also have the capability to measure beta doses or neutron doses arising from cosmic rays.

The dosimeters can be either active or passive devices, with some facilities employing more than one monitoring technique. Although active devices such as area monitors and electronic personal dosimeters are often used within a facility, passive systems are usually preferred for environmental applications because of their ease of deployment and the minimal maintenance required. Since the 1960s, thermoluminescence dosimeters (TLDs) have been used for environmental dosimetry applications, with the early systems using lithium fluoride (LiF) TLDs (Cusimano *et al* 1968).

Thermoluminescence (TL) is thermally stimulated light emission from an insulating material that has been exposed to ionizing radiation, and is a property of many natural minerals. Ionizing radiation can create electron-hole pairs in TL materials, which can either recombine or can become trapped at defects in the crystal structure. These trapped charge carriers are in a metastable state, and can be released by heating the material. The released charge carriers can then recombine, with an associated emission of light. By calibrating the amount of light released from the TLD after a known dose of ionizing radiation, the TL material can then possibly be used as a radiation dosimeter. The suitability of a given TL material for radiation dosimetry depends on a number of factors, including dose linearity, energy dependence, fading characteristics, and stability. Horowitz (1984a) presents a historical background and a more detailed description of the TL mechanism.

After initial research into LiF TLDs in the early 1960s at the University of Wisconsin, the Harshaw Chemical Company became the first commercial supplier of TLDs for radiation dosimetry, with the phosphor known as TLD-100 (Cameron 1970). The dopants present in the phosphor are necessary for desirable thermoluminescence (TL) properties, and TLD-100 denotes

a LiF crystal doped with trace amounts of magnesium and titanium. Later formulations used isotopically enriched ^{6}Li or ^{7}Li and these were denoted TLD-600 and TLD-700, respectively.

LiF TLDs are adequate for a wide range of applications at nuclear and radiological facilities, and are also used as radiation detectors in clinical dosimetry. For environmental applications the dose rates are generally very low, so several alternative TLD materials have been investigated that have much higher sensitivity than TLD-100. These phosphors include calcium sulphate ($CaSO_4$), calcium fluoride (CaF_2), and aluminium oxide (Al_2O_3), and each of these materials can be doped with different compounds to produce different dosimetric properties. The phosphors have photon sensitivities from 10 to 30 times greater than standard LiF, but the presence of higher atomic number elements make the dosimeters less tissue equivalent than LiF dosimeters. For example, for the same dose to tissue from 40 keV photons and ^{60}Co photons, the resulting dose to CaF_2 is 10 times higher for the 40 keV photons than the ^{60}Co photons. The dose to TLD-100 is only about 40% higher for the 40 keV photons than the ^{60}Co photons (Ranogajec-Komor *et al* 1993). It is possible to improve the sensitivity of TLD-100 by a factor of 5 using special irradiation and annealing methods (Horowitz 1984b), but these methods are fairly cumbersome for routine applications.

Nakajima *et al* (1978) presented a new type of LiF material that is doped with magnesium, copper, and phosphorus (LiF:Mg,Cu,P), and their results showed a photon sensitivity 23 times higher than TLD-100. The initial formulations suffered from poor reusability, but other groups improved on the stability of the phosphor, and a commercial version was available by the late 1980s (Pradhan and Bhatt 1989). Harshaw TLD, now known as Saint-Gobain Crystals and Detectors (SGC&D), began commercially producing LiF:Mg,Cu,P TLDs in the late 1990s, including versions with isotopically enriched ^{6}Li or ^{7}Li. The new materials are denoted TLD-100H, TLD-600H, and TLD-700H.

Perry *et al* (1999) describe a new environmental dosimetry system from SGC&D which uses either TLD-100H or TLD-700H, with four TLDs mounted in an assembly behind various filters. The filters provide energy discrimination capabilities so that the dosimeter can be used to measure the dose equivalent quantities relevant for environmental dosimetry. The holder design is a modification of previously existing ones used for personnel dosimetry and environmental

dosimetry, and the new holder with the LiF:Mg,Cu,P TLDs is denoted the Harshaw Type 8855 environmental dosimeter.

The 8855 dosimeter is designed to be used for environmental exposures to photon and beta sources, and Perry *et al* use the dosimeter for mean photon energies as low as 20 keV. To be able to determine the dosimetric quantities relevant to environmental dosimetry, namely the ambient dose equivalent, $H^*(10)$, and the directional dose equivalent, $H'(0.07,\alpha)$, the results from the multi-element dosimeter are processed through a neural network algorithm. Although the accuracy requirements for environmental dosimetry can be as high as 50%, the output from the neural network algorithm is quite sensitive to the element ratios, and the results can change by as much as 20% due to a change of only 5% in an individual element. To understand the energy response in the dosimeter under the various filters, it is necessary to have an understanding of the energy response of the TLD material itself. This knowledge can then lead to improvements in dosimeter designs in the future.

Two nuclear power utilities, Ontario Power Generation and Bruce Nuclear, have embarked on a joint research project to study the use of the 8855 dosimeter for their environmental dosimetry programs, with a large number of tests required to characterize the dosimeter. This project is a part of the larger study, and focuses on the photon energy response of the 8855 dosimeter, as well as the energy response of the bare TLD-100H chips. For comparison purposes, the photon energy response of TLD-100 is also examined.

1.1 Measurement Quantities

The following two radiation measurement quantities are used throughout the course of this work, and the reader should be familiar with these terms:

Kerma, *K*

Kinetic energy released per unit mass (J/kg). This non-stochastic quantity only applies for indirectly ionizing radiations, and is the expectation value of the energy transferred from uncharged particles to charged particles per unit mass at a point (Attix 1986). Kerma can be

defined in any medium, and the air kerma is related to the quantity *exposure*. The special unit of kerma is the gray (Gy).

Absorbed dose, *D*

Energy deposited per unit mass (J/kg). The absorbed dose is the expectation value of the energy imparted to matter per unit mass at a point (Attix 1986). The units are the same as kerma, but the difference between the two quantities is that dose is energy per unit mass that remains at point *P*, while the kerma is the kinetic energy per unit mass transferred to charged particles at point *P*. These particles may then leave the volume of interest, and produce none of the effects associated with ionizing radiation.

Although the ambient dose equivalent and the directional dose equivalent are the relevant quantities for environmental dosimetry, the absorbed dose is a more fundamental quantity that is useful for characterizing the intrinsic energy response of a dosimeter. For this reason, the environmental dose equivalents will not be further discussed in this work.

Response

For this work, the response is defined as the quotient of the TL signal and the dosimetric quantity that is being measured. The TL signal is integrated by the reader in units of charge (nC), and this value is divided by the relevant dosimetric quantity to calculate the response.

Air kerma response

The TL signal divided by the delivered air kerma. The relative air kerma response can be calculated by normalizing the results to one of the measurements, usually the response to ^{60}Co photons.

TLD dose response

The TL signal divided by the absorbed dose in the TLD. This is normally simply referred to as "dose response" throughout this work. The relative dose response can be calculated by normalizing the results to one of the measurements, usually the response to ^{60}Co photons.

Dose response in terms of medium

The TL signal divided by the absorbed dose that would be deposited in the medium in the absence of the TLD. This is not used in this work, but is used in many of the publications referenced throughout this work. Usually this is in terms of the TL signal arising from an absorbed dose in water or tissue.

Photon energy response

The air kerma response or dose response as a function of the photon energy, usually normalized to the ^{60}Co result.

1.2 Guide to the Thesis

The aim of this project was to test the photon energy response of the Harshaw Type 8855 environmental dosimeter. The energy response of the LiF:Mg,Cu,P (TLD-100H) bare chips used in the dosimeter was measured separately, and for comparison a duplicate set of measurements were performed using LiF:Mg,Ti (TLD-100).

Chapter 2 describes the air kerma response measurements for TLD-100 and TLD-100H, using the TLD system developed at the National Research Council Canada (NRC) (Janovský and Ross 1993). The previous work at the NRC focused only on the response of TLD-100 to ^{137}Cs and ^{60}Co γ-rays (Shortt *et al* 1997), and this work extends the measurements to mean photon energies as low as 24 keV.

Chapter 3 outlines the Monte Carlo simulations using EGSnrc (Kawrakow 2000) to calculate the absorbed dose to the TLDs for the measurements described in Chapter 2. Using these results, the dose response is calculated as a function of photon energy for both TLD-100 and TLD-100H. The results for both materials are compared to other published measurements of the energy response, and the correlation with ionization density is shown.

Chapter 4 describes the photon energy response measurements for the Harshaw Type 8855 dosimeter. Details of the protocol used to read the TLDs in the Harshaw TLD Model 6600 reader are presented, including a residual signal subtraction algorithm to improve the dosimeter

performance at low doses. EGSnrc Monte Carlo simulations of three of the dosimeter elements are also presented.

Chapter 2

Bare Chip Energy Response Measurements

2.1 Introduction

The photon energy response of TLD-100 has been measured by various groups since its development in the 1960s, with a compilation of data presented by Budd *et al* (1979). These studies focused on the response of TLD-100 to photons with energies from 20 to 200 keV, with the measurements expressed as the response in terms of dose to water, normalized to the ^{60}Co response. Although there was a great deal of scatter in the measurements, most of the groups measured a response in this photon range that was higher than what would be predicted based on the relative mass energy-absorption coefficients of TLD-100 and water. Horowitz (1984b) has suggested that the over-response is related to the increased ionization density at low energies, and that it may be related to the supralinearity behaviour of TLD-100 at high doses.

Published data on the photon energy response of TLD-100H is scarce since the material is fairly new, but Sáez-Vergara *et al* (1999) have compared its response to other available LiF:Mg,Cu,P formulations. Much more energy response data on the other formulations are available, and Olko *et al* (1993) have a series of publications characterizing the energy response of a Polish formulation of LiF:Mg,Cu,P.

The Ionizing Radiation Standards (IRS) TLD system has previously been described in detail (Janovský and Ross 1993), and the system was used in earlier work to characterize the response of TLD-100 to ^{137}Cs and ^{60}Co γ-rays (Shortt *et al* 1997). Due to the high level of precision achievable with the system, with a standard uncertainty of about 0.5%, it was used in this work to measure the energy response of TLD-100H bare chips. Measurements were performed for both TLD-100 and TLD-100H using ^{137}Cs and ^{60}Co sources, as well as a number of x-ray qualities using the ISO narrow spectrum series (ISO 1996).

2.2 Materials and Methods

All of the TLDs used in this work were obtained from Saint-Gobain Crystals and Detectors (SGC&D) (Solon, Ohio). The LiF:Mg,Ti (TLD-100) chips used previously at the National Research Council Canada (NRC) had a square cross section, and dimensions of 3.2 x 3.2 x 0.89 mm. In the present work, thinner TLD-100 chips were used, with dimensions of 3.2 x 3.2 x

0.38 mm. The LiF:Mg,Cu,P (TLD-100H) chips had a circular cross section, with a diameter of 3.6 mm and a thickness of 0.38 mm. The TLD-100 chips had a density of 2.64 $g \cdot cm^{-3}$, with Mg and Ti dopant concentrations of 200 and 10 ppm by weight, respectively[1]. The TLD-100H chips had a density of 2.48 $g \cdot cm^{-3}$, with P, Mg and Cu dopant concentrations of 3000, 2000 and 40 ppm by weight, respectively. Sets of 25 chips were stored in small quartz trays, and were kept at room temperature in a dark area when not in use.

The protocol used for the TLD-100 chips has been described previously (Janovský and Ross 1993, Shortt *et al* 1997), and will be briefly outlined here. The chips were annealed at 400°C in a high-temperature oven for one hour, with the quartz tray placed on a steel plate inside the oven. After the high-temperature anneal, the chips were rapidly cooled to room temperature by placing the tray on a brass block near the oven. After approximately 30 minutes, they were then annealed at 100°C in a low-temperature oven for two hours, and were again rapidly cooled to room temperature. After irradiation but prior to readout, the chips were annealed at 100°C in the low-temperature oven for 12 minutes. The post-irradiation anneal empties the low temperature traps, and reduces the effects of fading of the TL signal. The entire anneal/irradiation/readout process normally occurred over a period of less than 48 hours.

Temperature probes placed 3 to 4 cm above the quartz tray in each oven were used to maintain a constant air temperature. In addition, thermocouple probes were attached to the plates used to hold the quartz tray in each oven, so that the temperature could be measured in close proximity to the chips. The oven temperature settings were adjusted so that the probe in the steel plate was at the desired annealing temperature once it had achieved thermal equilibrium. The chips were only placed in the oven after the plate reached the equilibrium temperature, which took approximately two hours from a cold start for the 400°C oven, and one hour for the 100°C oven.

It is well known that LiF:Mg,Cu,P is much more sensitive to thermal treatment than LiF:Mg,Ti, with a reported irreversible loss in sensitivity if the material is heated much above

---

[1] Velbeck, K. J. (SGC&D) Private communication.

240°C (McKeever *et al* 1995). Horowitz and Horowitz (1990) report a loss of TL sensitivity of 20 – 50% after annealing samples for 10 minutes at 300°C, and the general recommendation for LiF:Mg,Cu,P is an anneal for 10 minutes at 240°C. Unfortunately, there is a high-temperature glow peak at approximately 270°C that cannot be fully read out without affecting the chip sensitivity. The residual signal is almost completely eliminated by annealing in an oven, but this cannot be done for TLD cards with chips mounted in Teflon®. The problems caused by residual signal for unannealed LiF:Mg,Cu,P are discussed further in Section 4.2.2.

The annealing protocol used for the TLD-100H chips was a modification of the one implemented at the CIEMAT Radiation Dosimetry laboratory (Sáez-Vergara and Romero 1996). The chips were annealed at 240°C for 15 minutes, followed by rapid cooling. Measurements were conducted in an attempt to estimate the actual temperature of the chips during the annealing process, by placing a thermocouple under the lid of the quartz tray (Figure 2.1). From these results, it can be estimated that the temperature of the chips was between 235°C and 240°C for approximately 10 minutes. Care was taken to place the quartz tray quickly inside the oven once the door was opened, because the temperature control system tended to overheat the oven temporarily if the temperature probe was allowed to cool more than a few °C. To prevent any overheating, the oven door was normally open less than 5 seconds. After irradiation but prior to readout, the chips were annealed at 130°C in the low-temperature oven for 12 minutes, followed by rapid cooling. Using this annealing process, the residual signal was reduced to less than 0.03%.

TLD readouts were performed using a Victoreen 2800M planchet-type reader, and the same time-temperature profile (TTP) was used for the TLD-100 and TLD-100H chips. At the beginning of the readout, the planchet temperature was increased to 100°C in approximately 2 seconds, and then increased linearly at $5°C \cdot s^{-1}$ to a maximum temperature of 240°C. The maximum temperature was maintained for 15 seconds, for a total readout time of 45 seconds. A continuous flow of nitrogen gas was used to purge the heating chamber, both during and after readout. The nitrogen reduces the background signal from the planchet, and also prevents oxidation of the TLD chip. Once the chip was placed on the planchet and the drawer was closed, a delay of 5 seconds prior to the beginning of the readout was used to allow the air to be purged

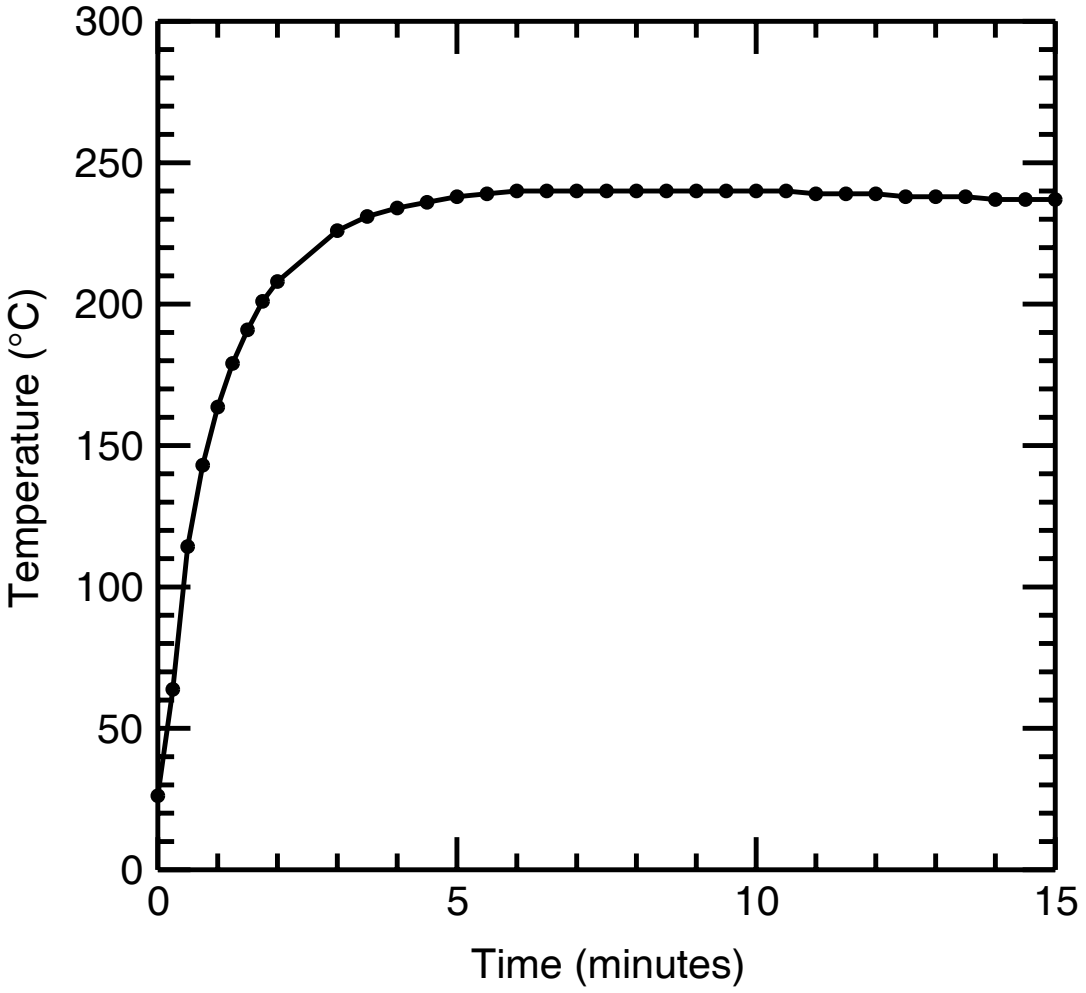

Figure 2.1: Temperature of the quartz tray during the 240°C anneal.

from the chamber. After readout, the planchet temperature was allowed to cool naturally to below 40°C before the planchet drawer was opened.

The TL glow curve was stored for each chip, with 450 data channels for the 45-second readout. The signal was integrated from channels 41 to 430 for both TLD-100 and TLD-100H. This corresponded to glow peaks 4 and 5 for TLD-100, and peak 4 and part of peak 5 for TLD-100H. The background signal would ideally be estimated by reading a freshly annealed chip immediately following every TLD readout, but since this was not practical, the background was estimated using readouts of the bare planchet. Several background measurements of the bare planchet were performed prior to reading each set of TLDs, using the same TTP and integrating region as was used for the TLDs. The average planchet background signal was calculated based on the three background measurements immediately before the first TLD was read. A background reading using a freshly annealed chip was approximately 10% higher than from the bare planchet, so the average background signal from the planchet was multiplied by 1.1 before applying the background subtraction. The background subtraction was equivalent to roughly 4 μGy air kerma from ^{60}Co when using TLD-100H, and 130 μGy air kerma from ^{60}Co when using TLD-100.

Each of the 25 chips was individually calibrated using ^{60}Co γ-rays in a field where the air kerma rate was accurately known. A polymethyl methacrylate (PMMA) phantom was used to hold all 25 chips for irradiation in the reference field, and the design is shown in Figure 2.2. The TLDs were placed symmetrically with respect to the front and back faces of the holder, with a wall thickness of 6 mm to provide charged particle equilibrium for the ^{60}Co source. Individual calibration factors for each chip were recorded after readout, and the TLDs were annealed again. The 25 chips were divided into groups of five, with subsequent irradiations performed in one of two smaller Lucite phantoms (Figure 2.2). The smaller phantoms were circular with a radius of 16 mm, and held five chips placed symmetrically about the central axis at a radius of 9 mm. One of the phantoms had wall thicknesses of 6 mm, and was used for the ^{60}Co and ^{137}Cs irradiations. The other phantom had wall thicknesses of about 1.6 mm, and was used for the x-ray irradiations.

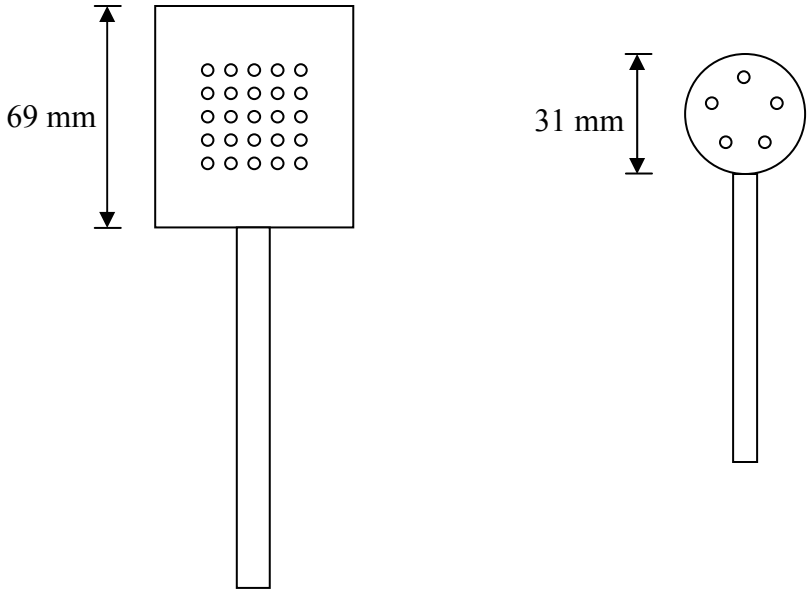

Figure 2.2: Phantoms used for the TLD irradiations. The large phantom was used for the initial calibrations, and the smaller phantom was used for the reference irradiation.

One group of five TLDs was irradiated in the ^{60}Co reference field to determine the overall change in sensitivity of the set. This change in sensitivity could result from the annealing process or by a change in the reader sensitivity. The other four groups were delivered graded exposures in the test beam, where the air kerma rate was also accurately known. After readout, the measured air kerma was determined for each chip using the TL signal and the ^{60}Co calibration factor. The result was divided by the known delivered air kerma to determine the air kerma response.

A description of the ^{137}Cs and ^{60}Co irradiation facilities at the NRC is presented by Shortt *et al* (1997). The air kerma rate for the ^{60}Co source has been determined using a graphite cavity chamber as a primary standard (Shortt and Ross 1986), and the ^{137}Cs air kerma rate was established using ionization chambers calibrated against the ^{60}Co primary standard. The ^{60}Co reference irradiations were performed using the Theratron Junior, at a distance of 3 m. The field size is 80 cm x 80 cm at this distance, and the air kerma rate is approximately $2.2 \cdot 10^{-2}$ mGy·s^{-1}. The x-ray air kerma rates are established using free air chambers, and the chambers are described by Henry and Garrett (1960). Special filters were used to provide the ISO narrow spectrum series x-ray beams used in this work. The irradiations were performed at 1 m from the source, where the field has a diameter of 15 cm.

2.3 Results and Discussion

Typical glow curves for TLD-100 and TLD-100H from ^{60}Co irradiations are presented in Figure 2.3. The TLD-100 glow curve was from a delivered air kerma of 17 mGy, while the TLD-100H glow curve was from a delivered air kerma of 1.3 mGy, and the TLD-100 results were scaled by a factor of about 2.6 so that the area under the two curves would be equal. For the protocols used in this work, TLD-100H was approximately 34 times more sensitive to ^{60}Co γ-rays per unit mass than TLD-100. The measured relative sensitivity is in broad agreement with other reported results, ranging from 10 to 35 times more sensitive than TLD-100 (Moscovitch 1999, Horowitz and Horowitz 1992). The large discrepancy in reported results is due to the fact that the measured sensitivity is dependent on many contributing factors, including the annealing and readout procedures used, the PMT spectral sensitivity, the optical properties of the chips, the reflectivity of the planchet, and the presence of encapsulation.

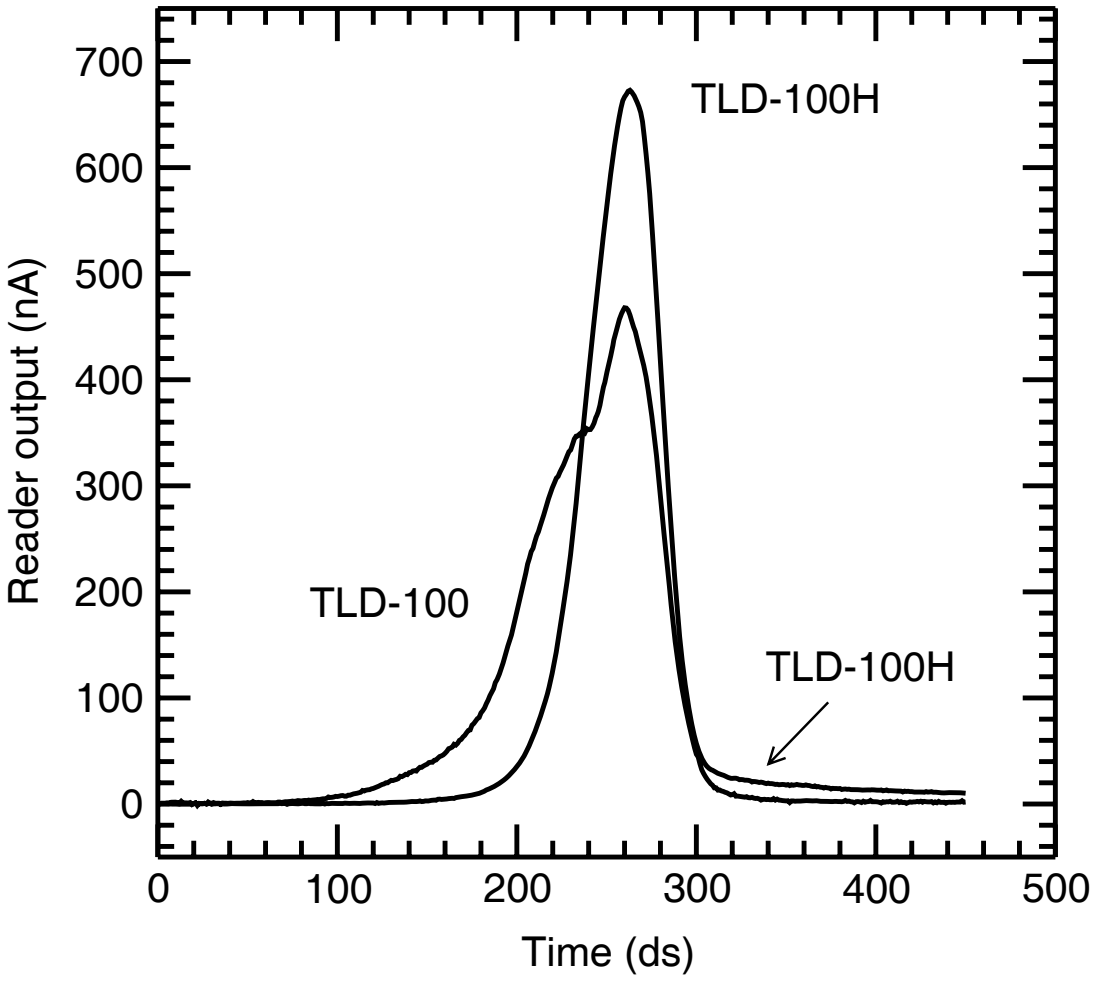

Figure 2.3: Typical glow curves for TLD-100 and TLD-100H. The air kerma values were 17 mGy and 1.3 mGy for TLD-100 and TLD-100H, respectively. The TLD-100 values were scaled by a factor of 2.57 so that the area under the two curves was equal.

A typical set of results from the air kerma response measurements is presented in Figure 2.4, for TLD-100H irradiations in the ISO 60 kV narrow spectrum beam (N-60), with the ^{60}Co irradiation results normalized to unity. The relative standard deviation in the response for each group of five chips was typically 0.4 – 0.6%, and was dependent on the photon beam energy and the type of TLD. As can be seen in the figure, the measured response was non-linear with respect to the delivered air kerma, with an increase in response as the air kerma was increased. For an increase in air kerma by a factor of 4, the response typically increased by 1 – 2%. This was measured for both TLD-100 and TLD-100H for all of the photon energies used, and was in disagreement with other reported results of the linearity of the two materials in this dose region. TLD-100 is known to exhibit supralinearity for absorbed doses between roughly 1 to 1000 Gy, but is reported to be linear for the air kerma range of 5 to 20 mGy used in this work (Horowitz 2001). TLD-100H has been reported to exhibit a linear dose response from 1 μGy to 1 Gy, with the measurable onset of saturation at about 10 Gy (Da-Ke *et al* 1984). Further measurements using TLD-100H in a different reader did not exhibit any non-linearity in this region, with the results presented in Figure 2.5. Although it is possible that the readout protocol used in the Victoreen 2800M reader may have led to these results, it is suspected that the measured non-linearity was an artefact of the reader. No experiments were conducted to demonstrate this conclusively, and no other planchet-type reader was available for testing, so all of the results were simply corrected for the measured non-linearity.

To calculate the response of the TLDs for each photon beam relative to the response to ^{60}Co, a linear least squares fit was performed on the test results, as shown in Figure 2.4. To correct for the non-linear response, the equation of the fitted line was used to calculate the air kerma delivery in the test beam that would be necessary to produce the same signal on the PMT as the ^{60}Co reference irradiation. The overall response to the test beam was then the ratio of this calculated air kerma level to the air kerma delivered from the ^{60}Co reference irradiation.

A summary of the test results is presented in Table 2.1 and Figure 2.6. The uncertainties for each test beam were calculated by combining the uncertainty in the least squares fit in quadrature with the uncertainty in the ^{60}Co reference results, for a typical uncertainty of 0.5% for TLD-100 and 0.7% for TLD-100H. These uncertainties are statistical only, and do not take into account any uncertainties in the source calibrations. The response results were in broad agreement with

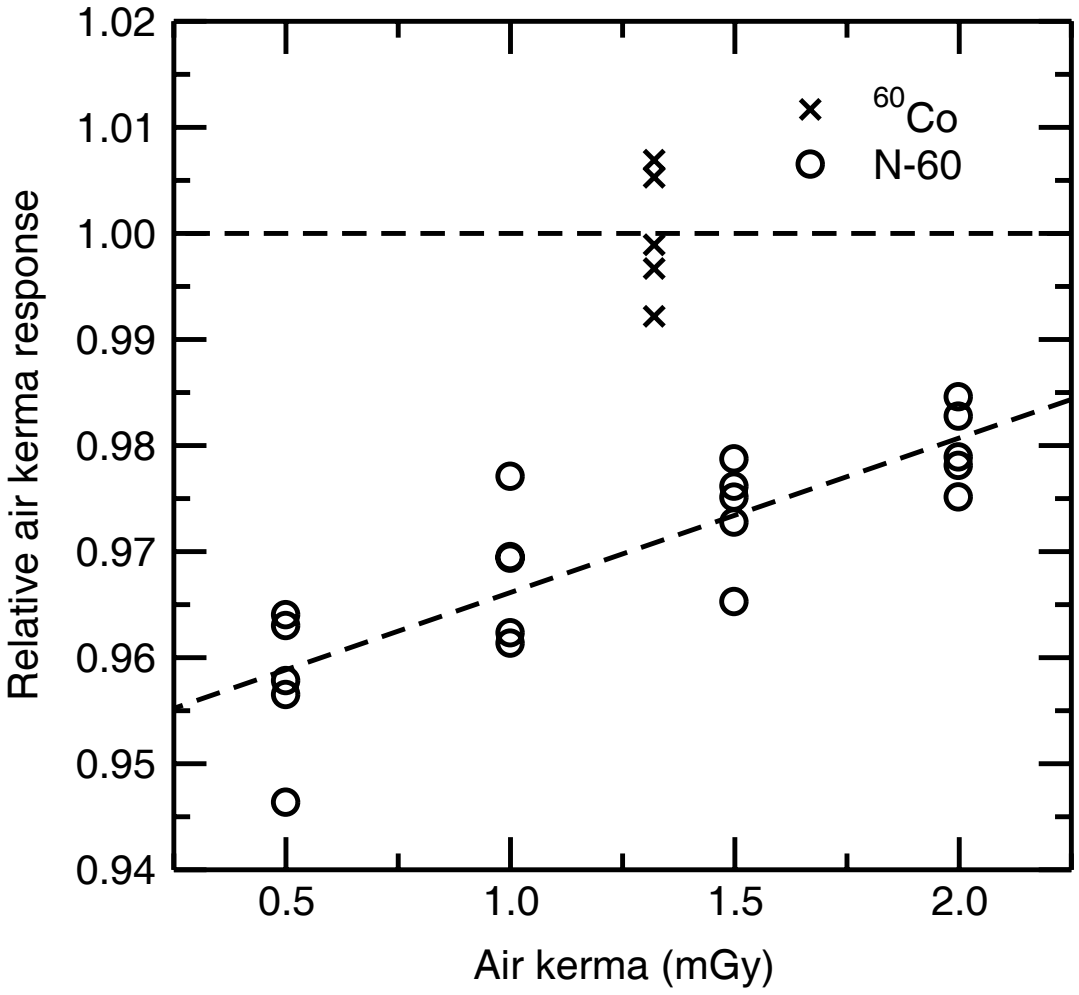

Figure 2.4: Typical set of air kerma response measurements. This set was for TLD-100H in the N-60 beam, with the ^{60}Co reference results shown.

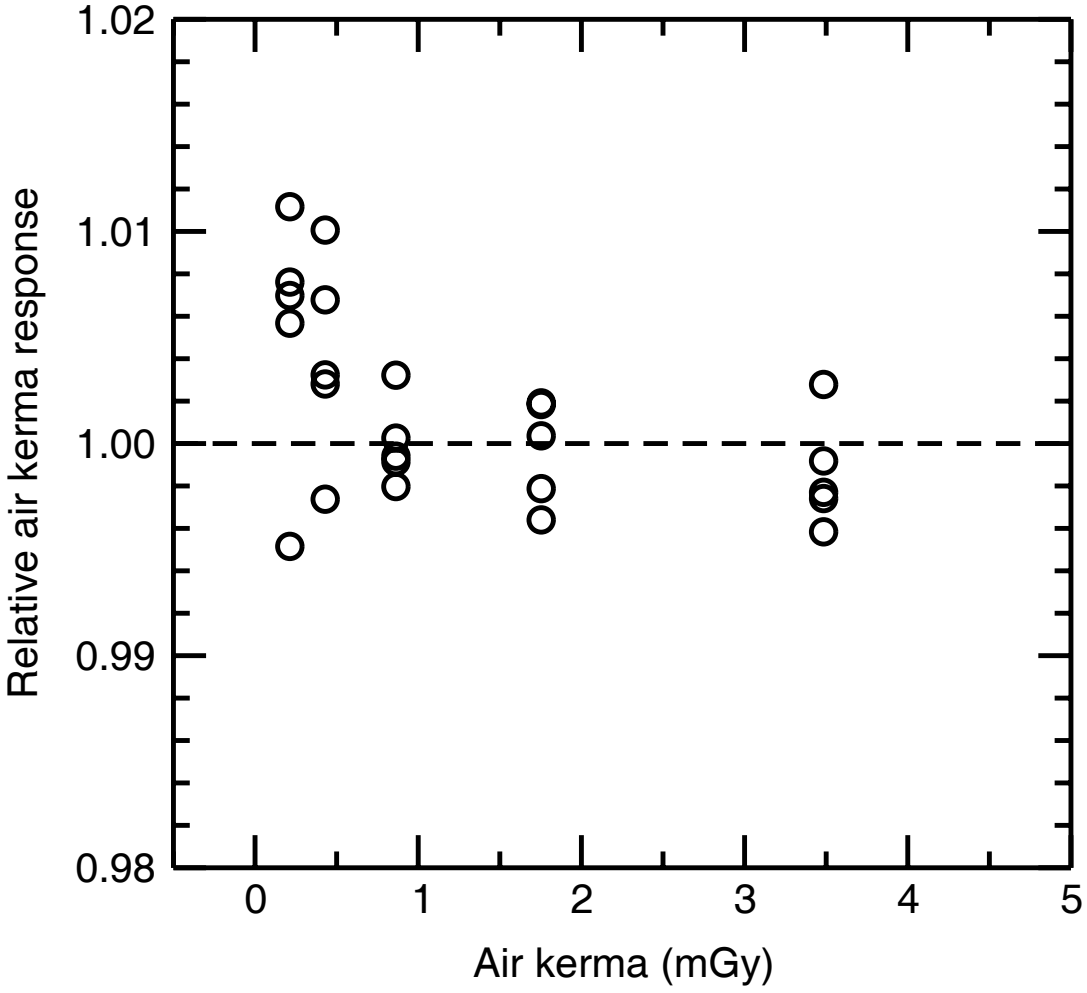

Figure 2.5: Linearity of TLD-100H in Harshaw Model 6600 hot gas reader, normalized to the mean response at 0.9 mGy.

Photon beam	Mean photon energy (keV)	Relative response (TLD-100)	Relative response (TLD-100H)
N-30	24	1.445(6)	0.941(6)
N-40	32	1.464(7)	1.014(7)
N-60	47	1.387(6)	0.971(7)
N-80	65	1.272(6)	0.846(6)
N-100	83	1.211(6)	0.778(3)
N-150	117	1.163(7)	0.775(5)
N-200	164	n/a	0.824(6)
N-250	207	1.110(7)	0.853(7)
^{137}Cs	612	1.023(6)	0.972(5)
^{60}Co	1055	1.000	1.000

Table 2.1: Measured air kerma response for TLD-100 and TLD-100H for several beam qualities. The mean photon energies listed for the ISO series x-ray spectra were calculated using tabulated spectra from GSF (Seelentag *et al* 1979), and the mean energies for ^{137}Cs and ^{60}Co were calculated using realistic spectra included in the EGSnrc Monte Carlo distribution (Rogers and Kawrakow 2000). The standard uncertainty in the last digit is given in parentheses.

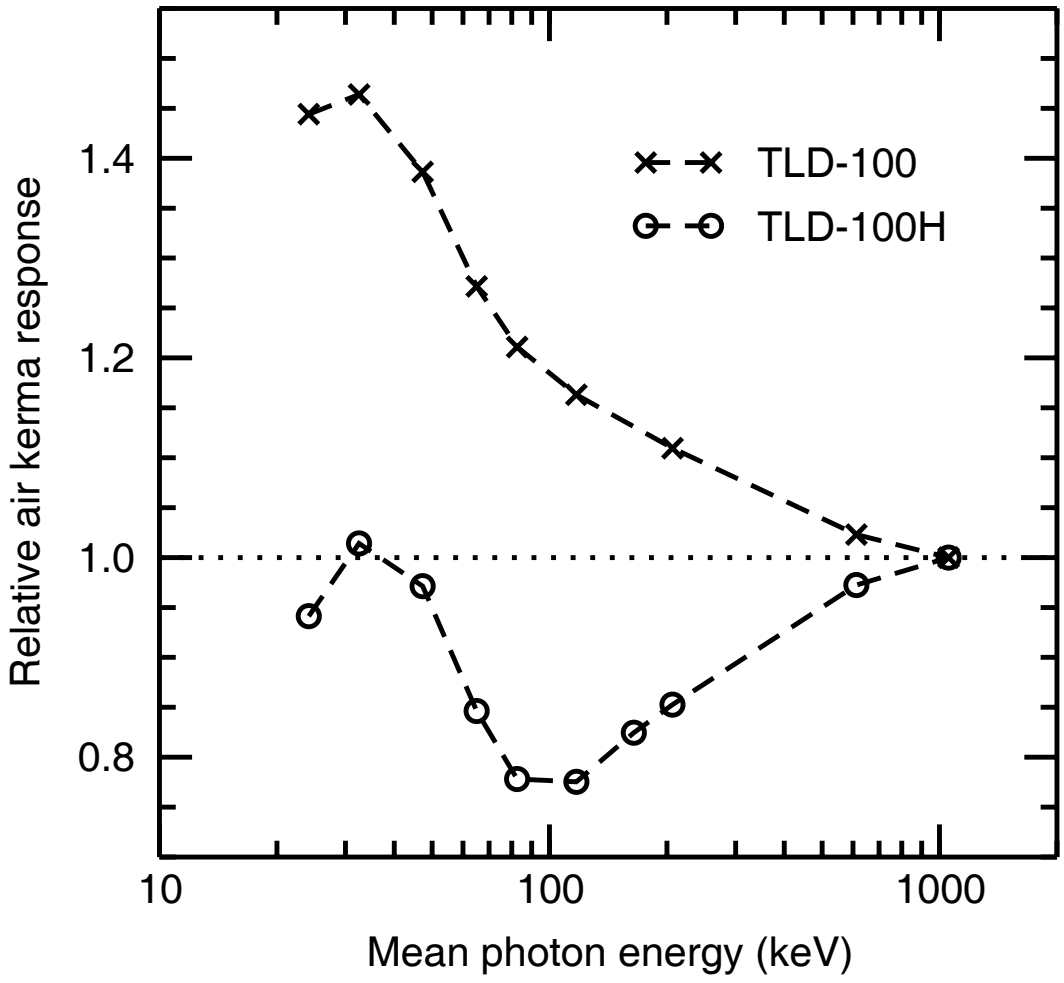

Figure 2.6: Air kerma response measurements for TLD-100 and TLD-100H. The standard uncertainty on each point is typically 0.5% for TLD-100 and 0.7% for TLD-100H.

other air kerma response measurements for both TLD-100 (Budd *et al* 1979), and TLD-100H (Olko *et al* 1993). Only one set of measurements was performed for each photon energy, so the uncertainty could have been reduced even further with repeated measurements.

Based on previous TLD studies conducted at the NRC (Shortt *et al* 1997), the measured air kerma response can be influenced by the phantom used for the irradiations, with photon attenuation and scatter occurring in the phantom. The earlier work at the NRC measured the response of TLD-100 to ^{137}Cs and ^{60}Co photons, and aluminium and PMMA phantoms with various wall thicknesses were used to measure the effect of photon attenuation and scatter in the phantom walls on the measured TL response. In this work, a different approach was taken using Monte Carlo simulations, and the calculations are described in detail in Chapter 3.

2.4 Conclusions

The energy response results were in broad agreement with other published results for both TLD materials, but these results are known to be influenced by the phantom used for the irradiations. Further calculations in the next chapter will determine the dose response as a function of energy.

Chapter 3

Bare Chip Monte Carlo Calculations

3.1 Introduction

In the previous chapter, the measurements of air kerma response were presented, but as demonstrated by Shortt *et al* (1997) the measured air kerma response can be influenced by the phantom used to hold the TLDs. It is preferable to determine the TLD dose response as defined in Section 1.1, so that the results can be compared with those obtained using different irradiation geometries and photon beams. A "perfect" TLD material would emit the same number of TL photons per unit of absorbed dose regardless of the beam quality, but due to the complex interactions that occur in TLD materials they may present non-linearity with respect to beam quality.

The calculation of absorbed dose in the TLD, given the delivered air kerma and the incoming photon spectrum, can be determined using various methods. Starting with a very simple model, we can assume that the phantom used to hold the TLDs is made of LiF, and that the wall of the phantom is thick enough to provide charged particle equilibrium at the position of the chips. We also neglect the presence of dopants in the TLDs in this simple model, and assume that the chips are made of pure LiF. We start with a parallel and monoenergetic incident photon beam, and assume that photon attenuation and scatter in the phantom can be neglected. The absorbed dose to the chip, D_{LiF}, is then given by

$$D_{\mathrm{LiF}} = \Psi \left(\frac{\mu_{\mathrm{en}}}{\rho} \right)_{\mathrm{LiF}}, \tag{3.1}$$

where Ψ is the photon energy fluence, and $(\mu_{\mathrm{en}}/\rho)_{\mathrm{LiF}}$ is the mass energy-absorption coefficient for LiF. The air kerma, K_{a}, for the same incoming photon beam is given by

$$K_{\mathrm{a}} = \Psi \left(\frac{\mu_{\mathrm{tr}}}{\rho} \right)_{\mathrm{air}}, \tag{3.2}$$

where $(\mu_{\mathrm{tr}}/\rho)_{\mathrm{air}}$ is the mass energy-transfer coefficient for air. This can then be expressed as

$$K_{\mathrm{a}} = \Psi \left(\frac{\mu_{\mathrm{en}}}{\rho} \right)_{\mathrm{air}} \frac{1}{(1-\bar{g})}, \tag{3.3}$$

where $(\mu_{en}/\rho)_{air}$ is the mass energy-absorption coefficient for air, and $\bar{g}$ is the fraction of incident energy lost to radiative processes. The radiative losses are important at high photon energies, but for the energy range used in this work $\bar{g}$ is never higher than 0.003, so it is neglected in the simple model. The resulting dose to the chips per unit air kerma is then

$$\frac{D_{\mathrm{LiF}}}{K_{\mathrm{a}}} = \left(\frac{\mu_{\mathrm{en}}}{\rho} \right)_{\mathrm{air}}^{\mathrm{LiF}}, \tag{3.4}$$

which is simply the ratio of mass energy-absorption coefficients for LiF to air.

Data for the mass energy-absorption coefficients of LiF and air were obtained from Hubbell and Seltzer (1997), and $D_{\mathrm{LiF}} / K_{\mathrm{a}}$ as a function of monoenergetic photon energy is presented in Figure 3.1. The theoretical dose to the TLD per unit air kerma is roughly constant at low photon energies, then drops by about 25% between 20 and 200 keV, and then remains constant up to 2 MeV.

For a slightly more realistic model, we need to consider that the actual phantom used in this work was made of PMMA, and not the LiF used in the simple model. The TLDs were 0.38 mm thick, and had a density of 2.5 to 2.6 g·cm^{-3}, for a density thickness of about 0.1 g·cm^{-3}. For the photon energies in consideration, the TLDs were too large to be considered Bragg-Gray cavities, where the dose is entirely deposited by electrons originating in the material surrounding the cavity. The density thickness of the TLDs was also less than the range of electrons produced from the ^{60}Co and ^{137}Cs beams, so the TLDs could not consistently be treated as "large" cavities either, where the dose is entirely deposited by electrons originating within the cavity. For these types of intermediate cavities, Burlin (1966) proposed that weighting factors could be used to reflect the two components of the electron spectrum, although several authors later pointed out shortcomings in Burlin's method (Horowitz *et al* 1983, Frujinoiu 2001, Mobit *et al* 1997). Since then, a number of different cavity theories have been proposed (Kearsley 1984, Haider *et al* 1997, Frujinoiu 2001), but they generally require the experimental determination of a number of parameters, or are only appropriate for simple one-dimensional geometries.

For realistic three-dimensional geometries, one must also consider the photon attenuation and scatter within the phantom and the chip itself, which can be simulated using Monte Carlo

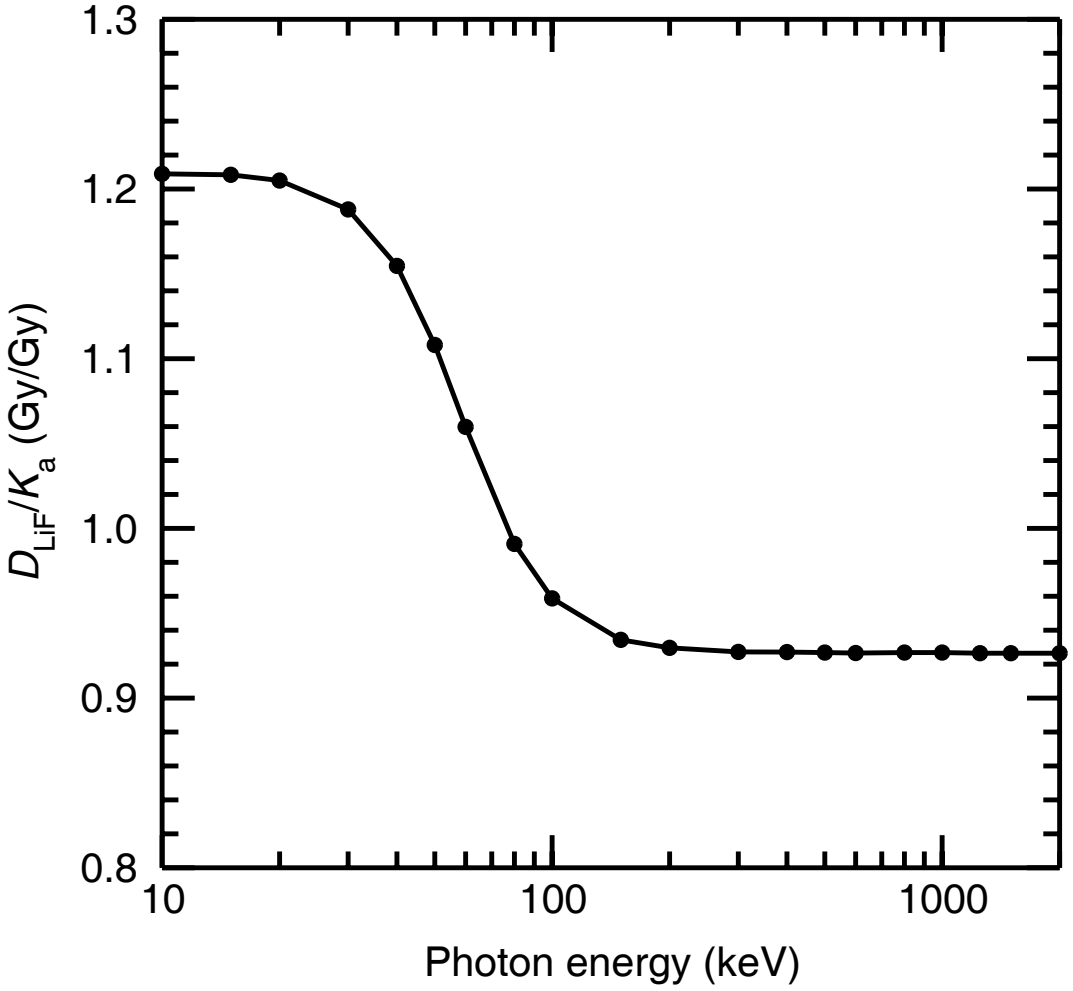

Figure 3.1: Calculated absorbed dose in LiF per unit air kerma as a function of photon energy. The TLDs were considered to be in a LiF phantom, and photon attenuation and scatter in the phantom was neglected.

techniques. Coupled photon-electron Monte Carlo codes can be used to calculate doses from photon sources directly, thus eliminating the need for a general cavity theory. In this work, the EGSnrc Monte Carlo system (Kawrakow 2000) was used to determine the dose to the TLDs per unit of delivered air kerma for each of the incident photon beams.

3.2 Background on EGSnrc

A historical look at the EGS (Electron Gamma Shower) system up to 1994 is available from Bielajew *et al* (1994), and a very brief history is presented here. Much of the early development of EGS took place at the Stanford Linear Accelerator Center (SLAC) at Stanford University, and the first major package was introduced in 1978, known as EGS3 (Ford and Nelson 1978). The system was designed to simulate electromagnetic cascades at energies from 100 GeV down to 1 keV for photons and 1 MeV kinetic energy for electrons. With the introduction of EGS4 in 1985, the low energy limit for electrons was extended to a kinetic energy of 10 keV (Nelson *et al* 1985). Several improvements were also made in the underlying physics, including the addition of Rayleigh scattering.

The transport of low energy electrons in EGS4 was improved with the introduction of PRESTA (Parameter Reduced Electron Step Transport Algorithm) in 1986 (Bielajew and Rogers 1987), and by 1989 the calculations of collision and radiative stopping powers were modified to be compliant with those from ICRU Report 37 (ICRU 1984). Several variance reduction techniques were also introduced to improve the efficiency of EGS4, including photon forcing, bremsstrahlung splitting, and electron range rejection (Rogers *et al* 1995).

A new version of EGS4, called EGSnrc, was released in 2000, and included major improvements in the electron transport methods in relation to EGS4/PRESTA (Kawrakow 2000). These improvements allowed EGSnrc to model ion chamber response at the 0.1% level, relative to its own cross sections. The low energy cutoffs were extended to 1 keV kinetic energy for both photons and electrons, but the performance at low energies is still under study.

Several user codes were developed over the years at the NRC to model cylindrical geometries for use with EGS3 and EGS4, and they have been updated for use with EGSnrc (Rogers *et al* 2001). These codes simplify the interface with EGSnrc, so that the user only needs

to change parameters in an input file to set up the appropriate geometry and scoring options. In this work, the DOSRZnrc code was used to calculate doses and air kerma, and the FLURZnrc code was used to calculate electron spectra in the TLDs.

This chapter presents the results from Monte Carlo simulations of the TLD holder used in Chapter 2, and uses the results along with the air kerma response measurements to calculate the dose response as a function of photon energy for both TLD-100 and TLD-100H.

3.3 Materials and Methods

3.3.1 Replacement of default photoelectric cross sections

As described in Section 3.2, much of the early work on the EGS system was performed in the 1970s, and much of the early code is still present in EGSnrc. During this early development, photon cross sections from Storm and Israel (1970) for elements 1 to 100 were implemented in the pre-processor for the shower codes. The cross sections were calculated quantities, and covered all of the major photon interactions, including pair production, coherent (Rayleigh) scattering, incoherent (Compton) scattering, and photoelectric absorption.

Since 1982, the National Institute of Standards and Technology (NIST) has compiled updated photon cross sections using different methods than Storm and Israel, with the most recent compilation published in 1999 (Berger *et al* 1999). Important differences between the two datasets appear for photoelectric interactions at photon energies lower than 200 keV, with up to 5% discrepancies in some cases (Hobeila and Seuntjens 2002).

The current version of EGSnrc uses the total photo-absorption cross sections from the PEGS4 pre-processor, which uses tabulated cross section data from Storm and Israel. PEGS4 calculates the total photo-absorption cross sections for compounds or mixtures by weighting the individual cross sections of the component elements based on their relative proportions in the material. The treatment of photoelectric interactions was modified substantially in the update from EGS4 to EGSnrc, with the option of explicitly simulating fluorescent photons and Auger electrons resulting from atomic shell vacancies. This was already implemented in a simplified

fashion in EGS4, but for mixtures or compounds it required the selection of an "effective" Z for the material, which was difficult for some materials where only a small fraction of a high-Z element was present (Kawrakow and Rogers 2001).

In EGSnrc, once a photoelectric interaction has been chosen based on the total cross section from PEGS4, the code needs to sample a specific element and atomic shell where the vacancy will take place to be able to simulate the relaxation particles correctly. To do this, EGSnrc uses the elemental composition information from PEGS4 along with its own fit formulas for the elemental cross sections, generated using photo-absorption cross sections from the NIST XCOM program (Berger *et al* 1999). The internal inconsistency in using different cross section datasets will likely be resolved in future versions of EGSnrc, with the revision of the PEGS4 pre-processor. This has not been a high priority to this point since the majority of EGS users work with photon energies in the range of 1 to 20 MeV, where photoelectric interactions have a relatively low probability of occurring.

To take full advantage of the recent NIST photo-absorption cross sections, the Storm and Israel photo-absorption cross sections normally used by PEGS4 were replaced by ones from XCOM, using a file provided by Hobeila[1]. Several tests were conducted to ensure that the new cross sections were working properly. For comparison purposes, two sets of PEGS4 material datasets were generated for each of the materials used in this work, one set using the XCOM photo-absorption cross sections, and the other set using the default Storm and Israel cross sections.

3.3.2 Creation of materials using PEGS4

New material data files were generated using PEGS4 for the Monte Carlo simulations of the TLDs in the PMMA phantom. The PEGS4 manual is included with the EGSnrc manual (Kawrakow and Rogers 2001), and describes in detail various operations that can be performed

[1] Hobeila, F. (McGill University) Private communication.

using the pre-processor. For this work, PEGS4 was simply used to generate the material data files using simple input files.

The compositions of the TLD materials, including dopants, were obtained from SGC&D, and the compositions of PMMA and air were obtained from the EGSnrc distribution. Natural isotopic abundances were used for all of the materials, including the TLDs, since TLD-100 and TLD-100H use natural lithium. The density and composition information for each of the materials used in this section are listed in Table 3.1. The density effect data from ICRU Report 37 (ICRU 1984), included with the EGSnrc distribution, were used when creating each of the materials, and the density effect data for pure LiF were applied for both TLD materials. The Rayleigh scattering option was turned on for all of the PEGS4 datasets, and the datasets were generated for photon and electron kinetic energy ranges from 1 keV to 2 MeV. As stated earlier, two separate sets of material datasets were generated, one using XCOM photo-absorption cross sections, and the other using Storm and Israel photo-absorption cross sections.

3.3.3 Calculation of air kerma

As stated in Section 3.1, the objective of the Monte Carlo calculations was to determine the dose to the TLDs per unit air kerma. The output from DOSRZnrc was in terms of dose delivered per unit of incident fluence at the surface of the modelled geometry, not per unit of air kerma, so it was necessary to determine the air kerma per unit of incident fluence as well. Monte Carlo simulations were performed using DOSRZnrc to score the air kerma from each of the incident photon beams, using a thin slab of air with a large radius and a parallel incident photon beam. This method was used by Borg *et al* (2000), and has the advantage of using a consistent set of underlying photon cross sections for the dose calculations and the air kerma calculations.

The dose to a 2 μm thick air slab with a 10 cm radius was scored for each of the incident photon beams, with the photons forced to interact in the slab. Tabulated photon spectra were used as inputs for the simulations, using data from GSF (Seelentag *et al* 1979) for the ISO narrow spectrum series x-rays, and data from the EGSnrc distribution (Rogers and Kawrakow 2000) for the ^{137}Cs and ^{60}Co beams. The spectral data from GSF for 30 kV to 150 kV were measured at a source-detector distance of 75 cm, and for 200 kV to 250 kV at a source-detector

Material	Density ($g \cdot cm^{-3}$)	Fractional composition by weight	
Air	$1.2048 \cdot 10^{-3}$	Carbon: Nitrogen: Oxygen: Argon:	$1.240 \cdot 10^{-4}$ $7.552 \cdot 10^{-1}$ $2.318 \cdot 10^{-1}$ $1.283 \cdot 10^{-2}$
PMMA	1.19	Carbon: Hydrogen: Oxygen:	$5.998 \cdot 10^{-1}$ $8.054 \cdot 10^{-2}$ $3.196 \cdot 10^{-1}$
TLD-100 (LiF:Mg,Ti)	2.64	Lithium: Fluorine: Magnesium: Titanium:	$2.670 \cdot 10^{-1}$ $7.328 \cdot 10^{-1}$ $2 \cdot 10^{-4}$ $1 \cdot 10^{-5}$
TLD-100H (LiF:Mg,Cu,P)	2.48	Lithium: Fluorine: Magnesium: Copper: Phosphorus:	$2.657 \cdot 10^{-1}$ $7.292 \cdot 10^{-1}$ $2 \cdot 10^{-3}$ $4 \cdot 10^{-5}$ $3 \cdot 10^{-3}$

Table 3.1: Composition of materials used in the Monte Carlo simulations. The air and PMMA compositions were obtained from the EGSnrc distribution, and the TLD compositions were obtained from SGC&D. Other possible impurities in the TLDs were not included.

distance of 225 cm. The cutoff energy for electron transport was raised to 2 MeV kinetic energy, so that the electrons were stopped as soon as they were created, and deposited all of their kinetic energy locally. The scored dose in the air slab was then equivalent to determining the air kerma. The photon transport cutoff was 1 keV, consistent with the value used for the dose calculations described in the next section, even though each photon only had a single interaction within the air slab.

All of the low energy options in DOSRZnrc were turned on for the simulations, including bound Compton scattering, Rayleigh scattering, and atomic relaxations. These options are described in detail in the EGSnrc manual. Each of the simulations used $1 \cdot 10^8$ histories, for a statistical uncertainty of about 0.01%, and a CPU time of approximately 30 minutes on a 733 MHz computer.

3.3.4 Calculation of TLD dose

In order to calculate the dose to the TLD chips inside the PMMA phantom, a model of the phantom geometry needed to be devised. A completely accurate three-dimensional model of the entire phantom was not practical using existing EGSnrc user codes, so some simplifications of the phantom geometry were necessary. To take advantage of the efficient and well-benchmarked cylindrical user codes at the NRC, the phantom was modelled as a cylinder with a single TLD chip embedded in the centre of the cylinder, with appropriate wall thicknesses in front of and behind the chip (Figure 3.2).

The real phantom did not have a uniform radius of PMMA around each of the TLDs, so the choice of an appropriate radius in the model phantom needed to be considered. Using the radius of the real phantom would lead to an overestimation of the contribution to the TLD dose from photons scattered in the phantom, and a small phantom radius could lead to an underestimation of the scatter component. To determine the sensitivity of the model to the phantom radius, several simulations were conducted using DOSRZnrc toexamine the dose delivered to the TLD chip as a function of the phantom radius. An alternate model was also created, using the real phantom radius and placing a ring of TLD material at the appropriate distance from the phantom

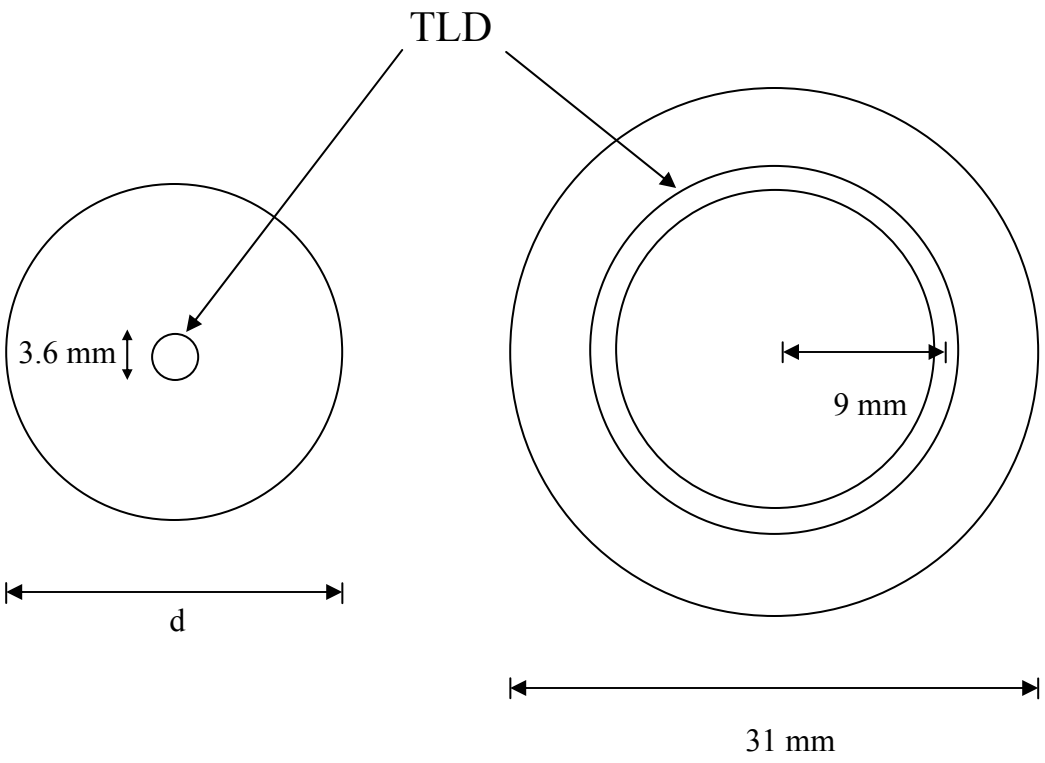

Figure 3.2: Model of phantom used for Monte Carlo calculations, for the centred chip and ring geometries.

axis (Figure 3.2). This model obviously distorted the shape of the TLDs, but was useful for comparison against the centred-chip model.

The various models were tested by simulating the geometry used by Shortt *et al* (1997) in earlier work performed at the NRC using TLD-100. The authors had performed a series of measurements to examine the effect of the front and back wall thickness of the phantom on the measured response, using ^{137}Cs and ^{60}Co photon beams. The simulations of these experiments were performed using DOSRZnrc, and only for the experiments that measured the change in TLD response in a PMMA phantom as a function of the front wall thickness. A discussion of the results from these simulations is presented in Section 3.4.1, and the outcome led to the selection of the phantom model to be used for the rest of the Monte Carlo simulations. The selected phantom model was a cylinder of PMMA with a radius of 13 mm, and a TLD with a 1.8 mm radius was embedded in the centre of the cylinder. Although the real TLD-100 chips actually had a square cross section, the area of the front face of the chips was the same as for circular chips with a 1.8 mm radius, so they were modelled in the same manner as the TLD-100H chips. For the phantom used in the x-ray beams, the front wall thickness was 1.63 mm and the back wall thickness was 1.87 mm. For the phantom used for the ^{137}Cs and ^{60}Co irradiations, the front wall thickness was 6.24 mm and the back wall thickness was 6.32 mm.

After the selection of an appropriate phantom model, a series of simulations were performed using DOSRZnrc for each of the photon beams used in this work. The photon sources were modelled as point sources at 1 m from the front face of the phantom, with a vacuum between the source and the phantom. The sources themselves were not explicitly simulated, but the source-phantom distance was entered so that a diverging photon beam was modelled at the front face of the phantom. It approximated the actual irradiation distance for the x-ray beams and the ^{137}Cs beam, but was smaller than the 3 m irradiation distance used for the ^{60}Co source. The phantom model only had a diameter of 26 mm, so the effect on the photon divergence by modelling the irradiation distance as 1 m instead of 3 m was negligible.

Unlike the air kerma calculations, electron transport within the phantom and TLD was simulated as well as photon transport, with an electron kinetic energy cutoff of 10 keV. The range of a 10 keV electron in water is only 3 μm (Johns and Cunningham 1983), which is small

when compared to the TLD and phantom dimensions, so it was appropriate to deposit the dose from a 10 keV electron locally. As with the air kerma calculations, the photon transport cutoff was 1 keV, which was the lowest energy allowed within EGSnrc.

All of the improved electron transport options in EGSnrc were turned on for the simulations, as well as all of the low energy photon and electron options. These options included the exact boundary crossing algorithm, the PRESTA-II electron-step algorithm, spin effects, NIST bremsstrahlung cross sections, bound Compton scattering, photoelectron angular sampling, Rayleigh scattering, and atomic relaxations. These options are described in detail in the EGSnrc manual. The photon forcing and electron range rejection variance reduction techniques were employed for the dose calculations, and these techniques are also described in detail in the EGSnrc manual.

The simulations were performed using TLD-100 and TLD-100H, and separate sets of simulations were performed using the XCOM photo-absorption cross sections and the Storm and Israel cross sections. All of the simulations were performed to a statistical uncertainty of less than 0.1%, requiring between $5 \cdot 10^8$ and $2.2 \cdot 10^9$ histories. The required CPU time for each simulation varied between 3 hours and 70 hours on a 733 MHz computer, depending on the photon energy and the phantom thickness.

3.3.5 Fluence calculations

Additional Monte Carlo simulations were performed to determine the electron fluence spectrum in the TLDs, to examine the relation between the electron spectrum and the measured energy response. The FLURZnrc user code was used for the simulations, which shares many of the same inputs as DOSRZnrc. The user code has various scoring options available, and for these simulations both the total electron fluence spectra and the primary electron fluence spectra were tabulated. The energy width of the scoring bins was modified depending on the incident photon energy, and the number of bins varied from 30 to 80 for all of the photon beams.

All of the options common to both FLURZnrc and DOSRZnrc were left unchanged, except for the electron transport cutoff. To be able to determine the contribution of low energy electrons to the fluence, the electron transport cutoff was lowered to 1 keV kinetic energy. This resulted in

longer calculation times per history, but good spectra were obtained using only $1 \cdot 10^7$ histories for each photon beam. The CPU time for each simulation varied between 0.5 hours to 7 hours on a 733 MHz computer, again depending on the photon energy and the phantom thickness. The FLURZnrc calculations were only performed using the XCOM photo-absorption cross sections.

3.4 Results and Discussion

3.4.1 Validation of phantom model

As described in Section 3.3.4, several different models of the phantoms used to hold the TLDs were simulated, in order to determine the one that most closely represented the real phantom. For the simple model with a single chip embedded in the centre of a PMMA cylinder, the sensitivity as a function of phantom radius was studied for several different photon beams, with some examples shown in Figure 3.3. For each of the examples, the results were normalized to the calculated dose to the TLD for a phantom with a radius of8 mm. In this way, the results from DOSRZnrc could be used directly, in terms of dose per unit of incoming photon fluence.

The results from the ISO narrow spectrum 60 kV beam (N-60) were the most sensitive to the phantom radius, with a 2.2% increase in the calculated dose for a phantom with 18 mm radius compared to the phantom with 8 mm radius. The increase in TLD dose for a larger phantom was due to Compton scattered photons from the sides of the phantom directed back towards the TLD. At high photon energies, Compton scattered photons tend to be scattered in the forward direction, but this tendency decreases as the photon energy decreases, with greater probability for photons with large scattering angles (Johns and Cunningham 1983). At very low photon energies, the photoelectric interaction predominates over Compton scattering, producing photoelectrons with a relatively short range. The N-60 beam had high enough photon energy so that many of the photon interactions in the sides of the phantom were Compton interactions, but low enough energy so that many of the Compton scattered photons had a large enough scattering angle to be directed towards the TLD.

Several simulations were also performed using a 16 mm phantom radius as in the real phantom, but with a ring of TLD material centred at 9 mm from the central axis. This model

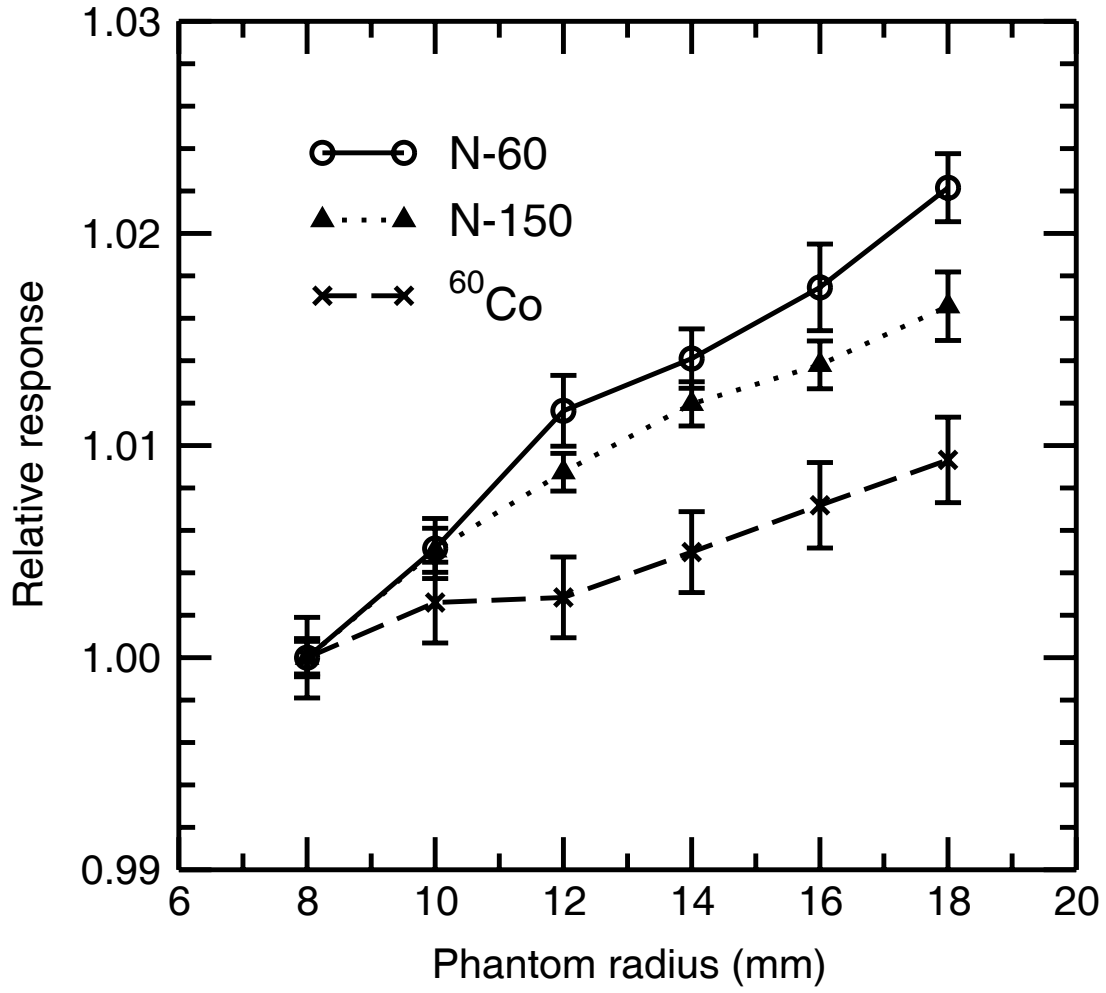

Figure 3.3: Calculated dose to the TLD as a function of phantom radius for several different photon beams. The results are normalized to the response for the 8 mm phantom radius.

maintained the cylindrical symmetry necessary for the user code, and correctly modelled the placement of the TLDs relative to the rest of the PMMA phantom, but distorted the shape of the TLDs themselves. For each of the photon beams, the ring model results corresponded well with a phantom radius of 13 mm in the centred-chip model.

In the earlier TLD work performed at the NRC (Shortt *et al* 1997) several measurements were performed using phantoms with different wall thicknesses, using ^{137}Cs and ^{60}Co photon beams. The TLD-100 chips used were thicker than in the current work, but the phantoms used for the irradiations had the same radius and TLD positions as the current phantoms. To test the validity of the various possible phantom models to be used in the Monte Carlo calculations, simulations of some of the experiments by Shortt *et al* were conducted and the results were compared to the experimental data. The dose to the TLD per unit incident fluence was divided by the calculated air kerma per unit fluence to determine the dose per unit air kerma for each of the front wall thicknesses, for both ^{137}Cs and ^{60}Co. A small $1/r^2$ correction was applied to the air kerma calculations to bring the point of measurement from the front face of the phantom to the centre of the TLD.

The experimental measurements from Shortt *et al* were in terms of air kerma response, normalized to the ^{60}Co response for a set of reference measurements. The experimental results as a function of PMMA front wall thickness are presented in Figure 3.4. The experimental results for each wall thickness were divided by the calculated dose per unit air kerma for that thickness, to determine the TLD dose response. One set of results is presented in Figure 3.5, using the calculated results for the phantom model with the radius of 13 mm, for both ^{137}Cs and ^{60}Co. The dose response should have been independent of the front wall thickness for any given photon beam, as long as the photon and electron spectra did not change much with increasing wall thickness. Least squares fits were performed on the ^{137}Cs and ^{60}Co datasets, with the resulting trendlines shown in Figure 3.5. For the 13 mm model, there appeared to be a slight under-response with increasing wall thickness for both of the sources, amounting to a 0.2% decrease from the thinnest to the thickest front walls. This suggested that the photon scatter in the phantom simulations might have been slightly overestimated, but would likely not have a large effect on the final results. For comparison, the results using the phantom with an 8 mm radius

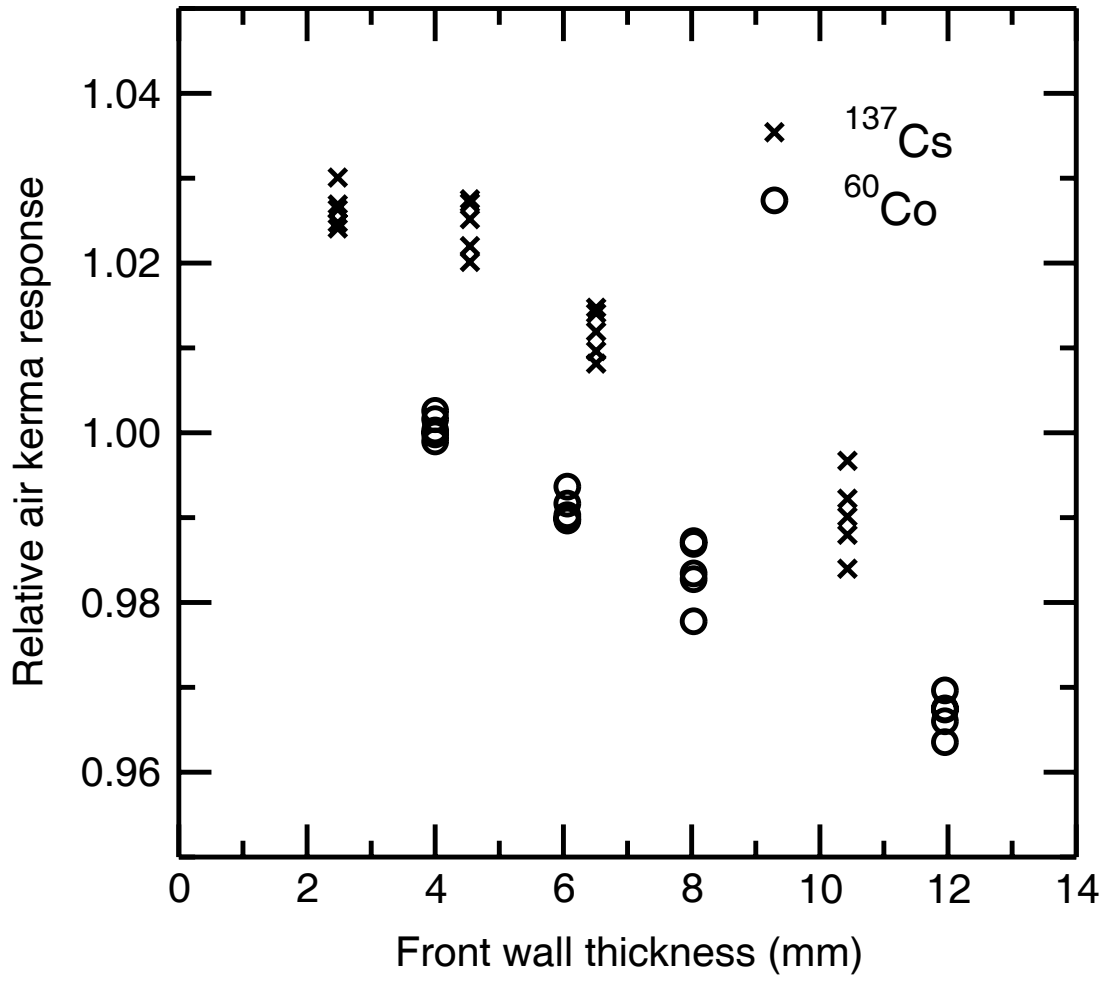

Figure 3.4: TL response as a function of PMMA front wall thickness (Shortt *et al* 1997).

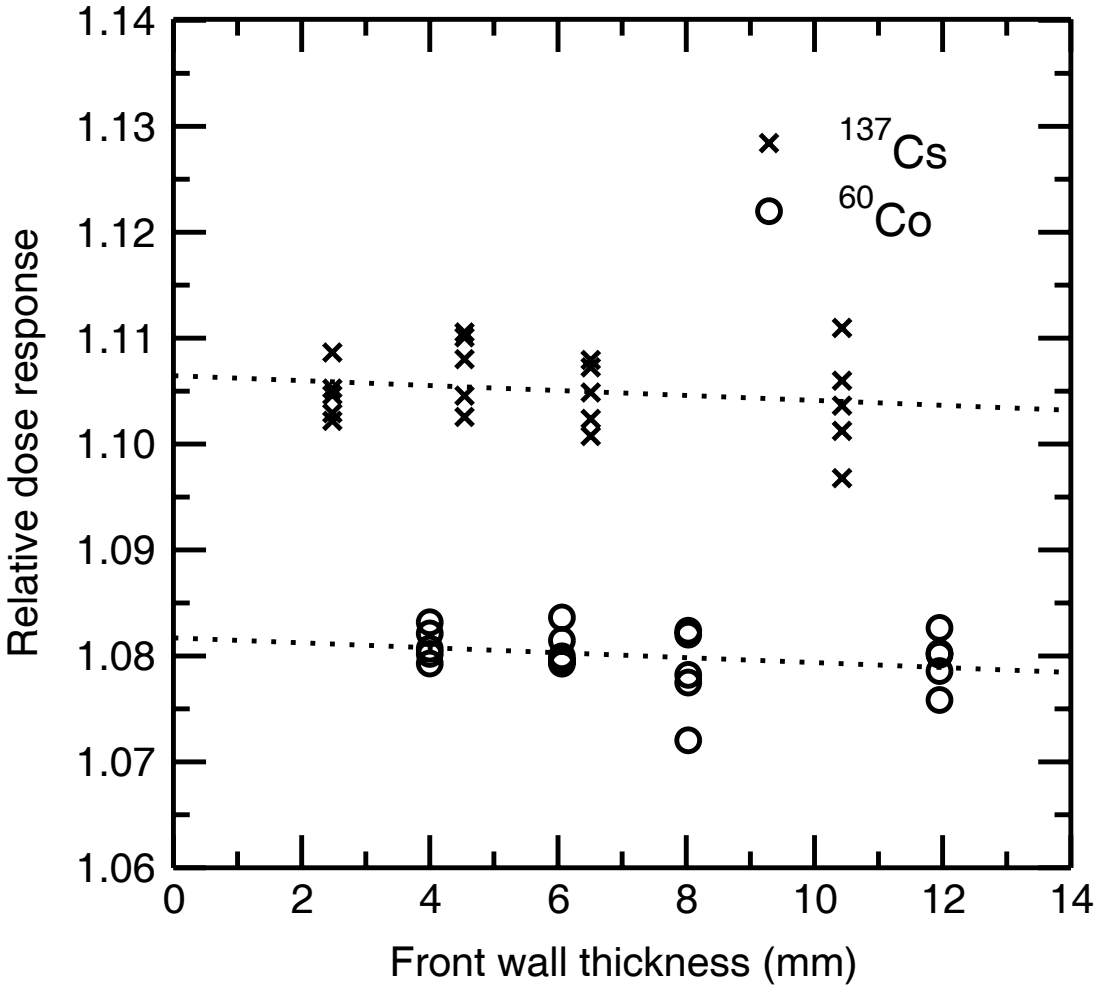

Figure 3.5: Measured TL response from Shortt *et al* per unit calculated dose, using a phantom model with a radius of 13 mm. A slight under-response of about 0.2% is evident for the thickest walls compared to the thinnest walls, which suggests that the calculated scatter component was overestimated.

produced an over-response of 1.1% from the thinnest to the thickest front walls, due to an underestimation in the scatter contribution.

Using the results from Figure 3.5, the ratio of the TLD dose response from ^{137}Cs to ^{60}Co was calculated to be 1.023 ± 0.002. This is in agreement with the measured ratio of 1.025 ± 0.007 from Shortt *et al*, using more measurement data and empirically derived correction factors for the front and back walls. In Shortt *et al*, the ratio was actually based on the air kerma response, which would be expected to be 0.1 – 0.2% higher for ^{137}Cs than for ^{60}Co based solely on the relevant mass energy-absorption coefficients.

Based on the good agreement between the experimental and calculated results, and the good agreement with the simulations using a ring of TLD material, the phantom model using a single centred chip and a 13 mm radius was used for the subsequent Monte Carlo simulations.

3.4.2 Dose calculation results

The results of the TLD dose calculations and the air kerma calculations are presented in Table 3.2 and Table 3.3, for TLD-100H and TLD-100 using both the XCOM and the Storm and Israel photo-absorption cross sections. A small $1/r^2$ correction was applied to the air kerma calculations to bring the point of measurement from the front face of the phantom to the centre of the TLD. The calculated doses per unit air kerma using the XCOM cross sections are presented in Figure 3.6, along with the predictions of the simple model described in Section 3.1. Error bars are not shown in the plot, since the statistical uncertainty on each of the points was only 0.1%.

The Monte Carlo calculated doses per unit air kerma for the ^{137}Cs and ^{60}Co beams were within 1% of the results from the simple model, which neglected photon attenuation and scatter within the phantom. For the lower photon energies, the Monte Carlo results were up to 12% higher than the predictions of the simple model. At low photon energies, scattered photons contributed a significant fraction of the dose to the TLD, but were not taken into account in the simple model. In addition, the presence of dopants in TLD-100H with higher atomic numbers than fluorine increased the probability for photoelectric interactions at low photon energies, which caused an increase in the deposited dose. The decrease in the calculated dose for the N-30 beam relative to the N-40 beam was mostly due to a decrease in the relative contribution from

Photon beam	Mean energy (keV)	K_a / Φ (Gy·cm^2)	$D_{TLD-100}$ / Φ (Gy·cm^2)	$D_{TLD-100H}$ / Φ (Gy·cm^2)	$D_{TLD-100}$ / K_a (Gy / Gy)	$D_{TLD-100H}$ / K_a (Gy / Gy)
N-30	24	$1.215 \cdot 10^{-12}$	$1.462 \cdot 10^{-12}$	$1.503 \cdot 10^{-12}$	1.208	1.242
N-40	32	$6.599 \cdot 10^{-13}$	$8.236 \cdot 10^{-13}$	$8.450 \cdot 10^{-13}$	1.253	1.285
N-60	47	$3.671 \cdot 10^{-13}$	$4.431 \cdot 10^{-13}$	$4.527 \cdot 10^{-13}$	1.211	1.238
N-80	65	$2.962 \cdot 10^{-13}$	$3.297 \cdot 10^{-13}$	$3.345 \cdot 10^{-13}$	1.117	1.133
N-100	83	$3.192 \cdot 10^{-13}$	$3.314 \cdot 10^{-13}$	$3.342 \cdot 10^{-13}$	1.042	1.051
N-150	117	$4.470 \cdot 10^{-13}$	$4.378 \cdot 10^{-13}$	$4.390 \cdot 10^{-13}$	0.983	0.986
N-200	164	$6.683 \cdot 10^{-13}$	$6.381 \cdot 10^{-13}$	$6.387 \cdot 10^{-13}$	0.958	0.959
N-250	207	$8.908 \cdot 10^{-13}$	$8.445 \cdot 10^{-13}$	$8.448 \cdot 10^{-13}$	0.951	0.952
^{137}Cs	612	$2.886 \cdot 10^{-12}$	$2.633 \cdot 10^{-12}$	$2.633 \cdot 10^{-12}$	0.924	0.924
^{60}Co	1055	$4.565 \cdot 10^{-12}$	$4.146 \cdot 10^{-12}$	$4.144 \cdot 10^{-12}$	0.920	0.919

Table 3.2: Results of TLD dose calculations and air kerma calculations using XCOM photo-absorption cross sections. The D/K_a values are corrected to the centre of the TLD, and have a statistical uncertainty of 0.1 %.

Photon beam	Mean energy (keV)	K_a / Φ (Gy·cm^2)	$D_{TLD\text{-}100}$ / Φ (Gy·cm^2)	$D_{TLD\text{-}100H}$ / Φ (Gy·cm^2)	$D_{TLD\text{-}100}$ / K_a (Gy / Gy)	$D_{TLD\text{-}100H}$ / K_a (Gy / Gy)
N-30	24	$1.177 \cdot 10^{-12}$	$1.425 \cdot 10^{-12}$	$1.465 \cdot 10^{-12}$	1.215	1.249
N-40	32	$6.422 \cdot 10^{-13}$	$8.032 \cdot 10^{-13}$	$8.244 \cdot 10^{-13}$	1.255	1.288
N-60	47	$3.605 \cdot 10^{-13}$	$4.345 \cdot 10^{-13}$	$4.440 \cdot 10^{-13}$	1.210	1.236
N-80	65	$2.939 \cdot 10^{-13}$	$3.271 \cdot 10^{-13}$	$3.317 \cdot 10^{-13}$	1.117	1.133
N-100	83	$3.178 \cdot 10^{-13}$	$3.297 \cdot 10^{-13}$	$3.324 \cdot 10^{-13}$	1.041	1.050
N-150	117	$4.461 \cdot 10^{-13}$	$4.366 \cdot 10^{-13}$	$4.378 \cdot 10^{-13}$	0.982	0.985
N-200	164	$6.678 \cdot 10^{-13}$	$6.374 \cdot 10^{-13}$	$6.380 \cdot 10^{-13}$	0.958	0.959
N-250	207	$8.906 \cdot 10^{-13}$	$8.436 \cdot 10^{-13}$	$8.438 \cdot 10^{-13}$	0.951	0.951
^{137}Cs	612	$2.885 \cdot 10^{-12}$	$2.634 \cdot 10^{-12}$	$2.633 \cdot 10^{-12}$	0.924	0.924
^{60}Co	1055	$4.565 \cdot 10^{-12}$	$4.144 \cdot 10^{-12}$	$4.142 \cdot 10^{-12}$	0.919	0.919

Table 3.3: Results of TLD dose calculations and air kerma calculations using Storm and Israel photo-absorption cross sections. The D/K_a values are corrected to the centre of the TLD, and have a statistical uncertainty of 0.1 %.

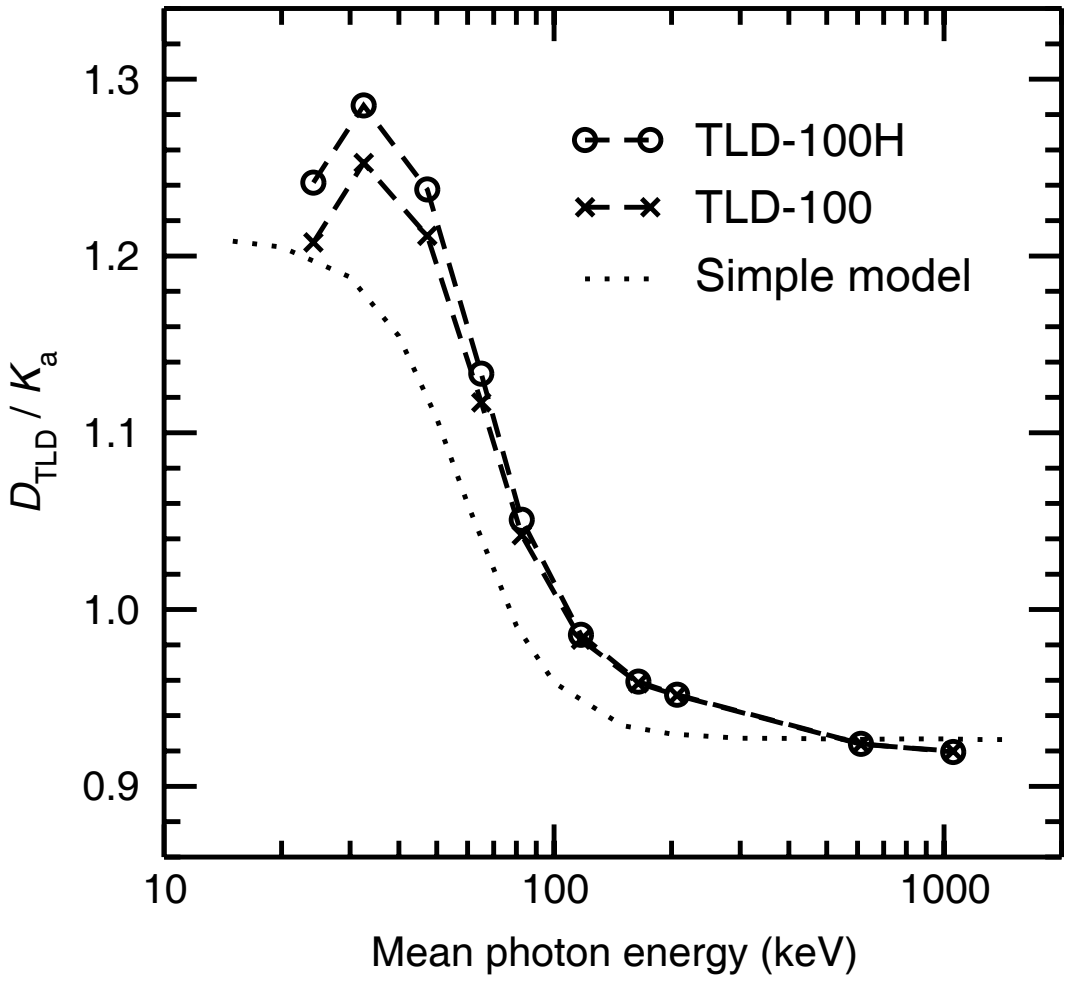

Figure 3.6: D_{TLD} / K_a for TLD-100 and TLD-100H, compared with the prediction from the simple model, using the XCOM photo-absorption cross sections. The statistical uncertainty on each point is 0.1%.

scattered photons, and partly due to an increase in photon attenuation in the front wall of the phantom.

Although the use of the different sets of photo-absorption cross sections led to differences of up to 3% for some of the individual calculations, most of these discrepancies cancelled out with the calculation of the dose per unit air kerma. The final result was a ratio of two sets of calculations using the same underlying set of cross sections, so the differences between the final results were only up to 0.6%. This was encouraging, since it implied that the choice of cross section dataset was not critical for this specific set of calculations, and did not dominate the uncertainty in the final results.

3.4.3 TLD dose response

The measured air kerma response results presented in Section 2.3 were divided by the calculated TLD dose per unit air kerma in the last section, to obtain the TLD dose response for each of the photon beams. The results are presented in Table 3.4 and Figure 3.7, normalized to the ^{60}Co response, for both TLD-100 and TLD-100H. The differences between the results using the different sets of photo-absorption cross sections were small, so only the results using the XCOM cross sections are shown. The stated uncertainties were calculated by adding the statistical uncertainties in the Monte Carlo calculated values in quadrature with the uncertainties from the experimental measurements.

TLD-100

Although the two TLD materials are chemically similar, it is clear that their dosimetric properties are dramatically different. As discussed in Section 2.1, several groups have studied the energy response of TLD-100 since its development in the 1960s, with a compilation of results presented by Budd *et al* (1979). The current results are in reasonable agreement with the compilation from Budd *et al*, and the energy response trend from Tochilin *et al* (1968) is shown in Figure 3.8. The uncertainties on the measurements by Tochilin *et al* were typically about 5%, and a smooth trendline was used to illustrate the measured dose response.

Photon beam	Mean photon energy (keV)	Relative response (TLD-100)	Relative response (TLD-100H)
N-30	24	1.100(5)	0.697(4)
N-40	32	1.075(5)	0.726(5)
N-60	47	1.053(5)	0.722(5)
N-80	65	1.047(5)	0.687(5)
N-100	83	1.069(6)	0.681(3)
N-150	117	1.089(6)	0.723(5)
N-200	164	n/a	0.790(6)
N-250	207	1.073(7)	0.829(7)
^{137}Cs	612	1.018(6)	0.968(5)
^{60}Co	1055	1.000	1.000

Table 3.4: Dose response for TLD-100 and TLD-100H. The standard uncertainty in the last digit is given in parentheses (statistical only). The results were calculated by dividing the air kerma response measurements by the calculated dose per unit air kerma.

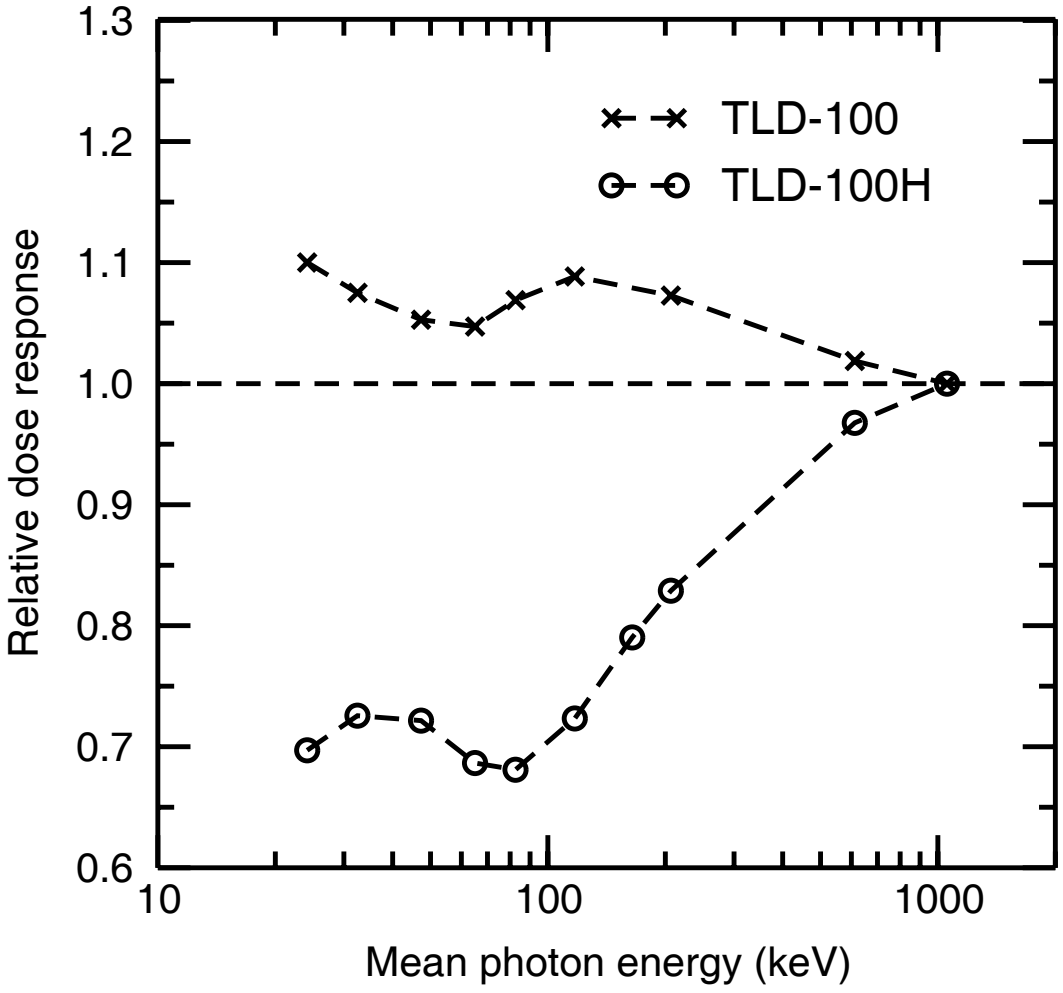

Figure 3.7: Dose response for TLD-100 and TLD-100H, normalized to ^{60}Co. The standard uncertainty on each point is typically 0.5% for TLD-100 and 0.7% for TLD-100H. The results were calculated by dividing the air kerma response measurements by the calculated dose per unit air kerma.

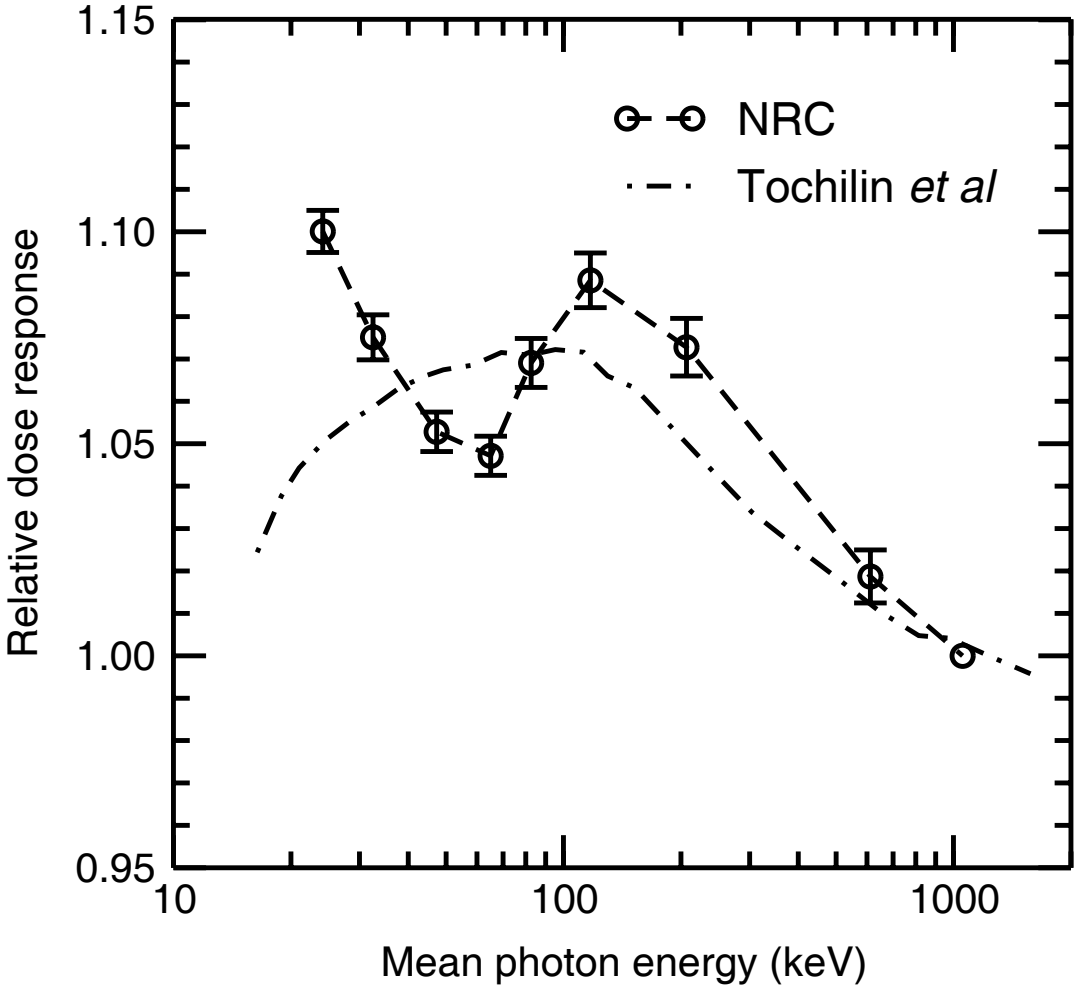

Figure 3.8: Comparison of current energy response results for TLD-100 with results from Tochilin *et al* (1968). The uncertainties in the current data are shown, and are typically 0.5%.

The increase in TLD-100 response with decreasing photon energy can be explained qualitatively within the framework of the unified interaction model (UNIM) proposed by Horowitz (2001), and is related to the ionization density of the photon beams. The UNIM can explain many features of TLD-100 response, including its supralinearity at high doses and the dependence of the supralinearity on the ionization density of the radiation. Most of the features are explained as a result of competitive mechanisms during the heating stage, with a dependence on the spatial distribution of trapped electrons and holes in the absorption stage. Spatially correlated electron-hole pairs are less influenced by these competitive processes, and are more likely to occur with increased ionization density. Although Horowitz does not explicitly discuss the energy response of TLD-100 at low doses with respect to the UNIM, he has used this qualitative explanation in earlier work (Horowitz 1984b).

For high-LET radiations, such as heavy charged particle beams, TLD-100 is known to under-respond per unit absorbed dose relative to its ^{60}Co response (Horowitz *et al* 2001). This is explained in the UNIM as a result of localized saturation of the relevant trapping and recombination centres along the particle tracks. Several authors have measured a decrease in the response from TLD-100 for photon energies below 20 keV relative to its ^{60}Co response (Gamboa-deBuen *et al* 1998, Tochilin *et al* 1968), and this may also be due to localized saturation with increasing ionization density. In this work, the lowest energy x-ray beam had a mean photon energy of 24 keV, and the saturation effects were not directly observed in TLD-100, although the results from Tochilin *et al* had started to demonstrate a decreasing response at a comparable energy.

The energy response shown in Figure 3.7 correlated fairly well with the mean ionization density of the photon beams, and the observed structure in the 60 – 120 keV region reflected the change in the proportion of photoelectric interactions to Compton interactions. This structure was more clearly visible in the TLD-100H measurements, so it will be explained in detail when discussing those results.

The energy response results challenge the conclusion of Das *et al* (1996) that the response of TLD-100 is directly proportional to absorbed dose in the TLD, and is independent of beam quality. Das *et al* were assessing the accuracy of Monte Carlo simulations to predict the energy

response of TLDs and diodes, and used four photon beam qualities to reach this conclusion. The lowest beam had an effective energy of 19 keV, and the highest energy was from a 4 MV linear accelerator. The uncertainties on their TLD data were from 1.6 to 6.7%, and their Monte Carlo calculations relied on cavity theory to calculate the dose to the TLDs. The source of the discrepancy is not clear, but warrants further investigation, since the conclusion implies that the response of TLD-100 can be calculated directly using Monte Carlo simulations, without taking into account the intrinsic energy response. Based on the current results, this could lead to errors of up to 10% on the calibration of ^{125}I and ^{103}Pd sources used in brachytherapy.

TLD-100H

The energy response of LiF:Mg,Cu,P has been studied in detail by Olko *et al* (1993), at the Institute of Nuclear Physics (INP) laboratory in Krakow, Poland. The Polish version of LiF:Mg,Cu,P is denoted MCP-N, and has a 30 times higher concentration of copper and 2.3 times higher concentration of phosphorus relative to TLD-100H. Even though the dopant concentrations were different, the measured energy response of TLD-100H was in good agreement with the measured energy response of MCP-N, as shown in Figure 3.9. An early paper by Shoushan *et al* (1986) described the energy response of LiF:Mg,Cu,P as "abnormal", and Pradhan and Bhatt (1989) described it as "anomalous" since it was very clear that the measured air kerma response did not correspond well with the change in mass energy-absorption coefficient, unlike TLD-100. Pradhan and Bhatt suggested that the energy response could be related to the LET of the photon beam.

Olko *et al* present a phenomenological model to explain the behaviour of LiF:Mg,Cu,P by relating the TLD dose response, or TL efficiency, to the frequency-mean lineal energy ($\overline{y}_F$) in the TLD. Lineal energy is a microdosimetric stochastic quantity, and is calculated as the amount of energy deposited in a defined volume divided by the mean chord length of the volume. Lineal energy is similar to the more common linear energy transfer (LET), but it can explicitly take into account energy loss straggling, the effect of delta electrons, and the curved tracks of slow electrons. To calculate $\overline{y}_F$ for a given photon beam, Olko *et al* used the Monte Carlo code Phoel-2 (Turner *et al* 1980) to determine the primary electron spectrum in the TLD arising from Compton or photoelectric interactions within the chip. The microdosimetric Monte Carlo code

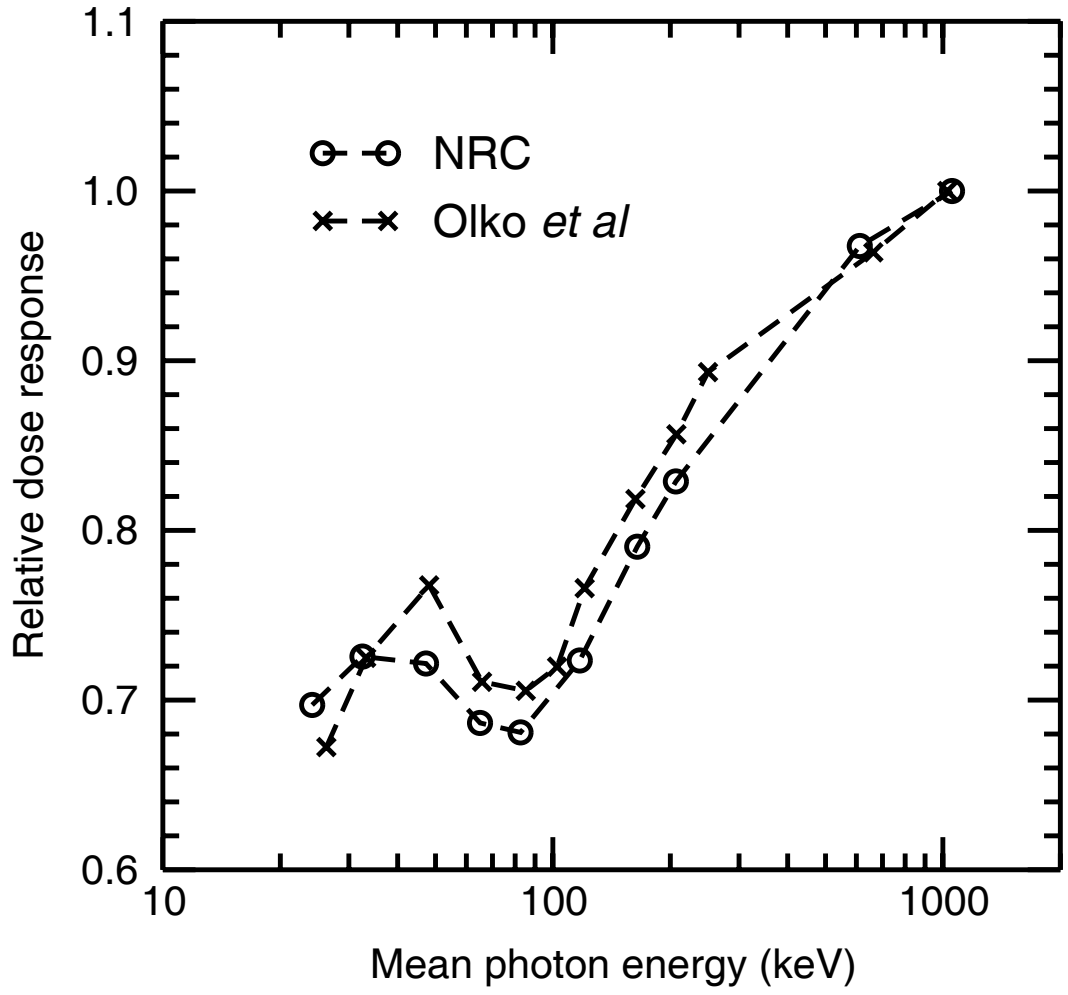

Figure 3.9: Comparison of current energy response results of TLD-100H with results from Olko *et al* (1993).

MOCA-8 (Olko and Booz 1990) was used to score lineal energy in an arbitrary target volume of water vapour from monoenergetic electrons, and was able to transport electrons with energies lower than 100 eV. The frequency-mean lineal energy, $\overline{y}_F$, was calculated by weighting the y_F^i for monoenergetic electrons of energy e_i based on their relative contribution to the dose. It was implicitly assumed that the y_F values generated in water vapour could be related to LiF:Mg,Cu,P simply by scaling the density. Although not explicitly stated in the paper, it appears that a target diameter of 40 nm in the TLD was chosen because it produced a nearly linear relationship between $\overline{y}_F$ and the TL efficiency. The change in TL efficiency with lineal energy was simply described as an "ionization density effect".

In a later paper by Olko *et al* (1994), the target diameter was modified to 35 nm, and the choice of target diameter was related to the response of LiF:Mg,Cu,P at high doses, with a sub-linear response reported to begin at about 10 Gy. It was also suggested that the target diameter could be related to the average distance travelled by an electron released from its trap before reaching a luminescent centre. Another paper by Olko (1996) extended the model to cover beta particles, thermal neutrons, and alpha particles. In this paper, the target diameter was modified to 24 nm. The ionization density effect was explained as a localized saturation in the region of the particle track. This explanation is similar in nature to the localized saturation proposed by Horowitz in the UNIM as applied to heavy charged particle tracks (Horowitz *et al* 2001).

The early saturation of TLD-100H at high doses compared with TLD-100, along with the lack of supralinearity at high doses for TLD-100H, support the suggestion that the photon energy response of both materials is a consequence of ionization density effects. For higher energy photons, the response at high doses is affected by the interaction between separate ionization tracks, while at low doses the same effect can be seen in a single track for low energy photons that produce higher ionization density.

As EGSnrc is a general-purpose Monte Carlo package, it is not intended to model electron transport at energies below 1 keV, where the cross sections for most materials are not well known. Another general purpose Monte Carlo package, PENELOPE, has been successfully used for transport of electrons with kinetic energies as low as 100 eV (Stewart *et al* 2002), but for lower energies specialized microdosimetric Monte Carlo codes such as MOCA-8 are generally

necessary. These microdosimetric codes are much more computationally demanding, since they simulate charged particle transport on an event-by-event level. Most of the simulations are also performed in water, since accurate cross sections for most other materials are unavailable. For this reason, EGSnrc was not used to calculate $\bar{y}_F$ using the methodology presented by Olko *et al*.

It was possible to score the electron spectra produced in the TLDs by each of the photon beams using FLURZnrc, and example spectra for the N-60 and N-100 beams are shown in Figure 3.10. These spectra were used to calculate the mean electron energies and the mean restricted mass collision stopping powers ($\bar{L}/\rho_{coll}$) produced by each of the photon beams, with the results for TLD-100H shown in Figure 3.11. The L/ρ_{coll} values for monoenergetic electrons in the TLDs were obtained from the PEGS4 datasets using the EXAMIN user code, and the mean stopping powers were calculated by weighting the L/ρ_{coll} values with the relative electron fluence. The electron cutoff energy in the simulations was 1 keV, so it was not possible to account for electrons below the cutoff. This artefact meant that the mean electron energies were somewhat overestimated and the $\bar{L}/\rho_{coll}$ values were likely underestimated.

At photon energies below 200 keV, on average less than 20% of the incoming photon's energy is transferred to an electron produced from a Compton interaction, and this fraction is even lower for low energy photons (Johns and Cunningham 1983). In contrast, a photoelectron will receive all of the kinetic energy of the incident photon, minus its atomic binding energy. As shown in Figure 3.11, as the photon energy decreased and the proportion of photoelectric interactions increased significantly relative to the Compton interactions, there was actually a slight rise in the mean electron energy. The $\bar{L}/\rho_{coll}$ values demonstrated a similar behaviour in the opposite direction, since higher energy electrons result in a lower mean stopping power.

The $\bar{L}/\rho_{coll}$ values were used as a measure of the LET of the photon beams, and the dose response as a function of $\bar{L}/\rho_{coll}$ is presented in Figure 3.12 for TLD-100 and TLD-100H. Although there is a clear correlation between the stopping power and the dose response for both materials, the relationship is less clear for $\bar{L}/\rho_{coll}$ values between 11 – 14 MeV·cm^2·g^{-1}. Based on the results of Olko *et al*, the dose response is likely better described using $\bar{y}_F$ than $\bar{L}/\rho_{coll}$.

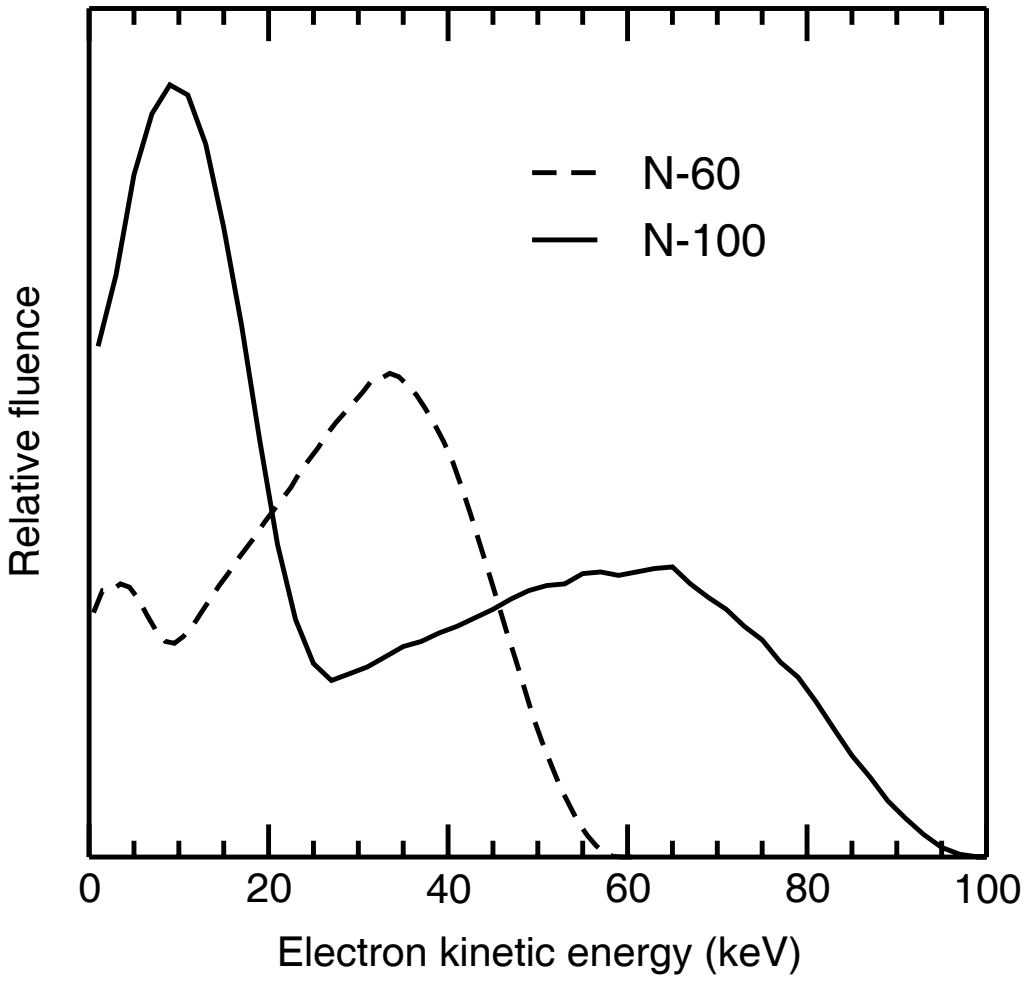

Figure 3.10: Electron spectra from FLURZnrc resulting from the N-60 and N-100 beams. The results are normalized to the same area under each of the curves.

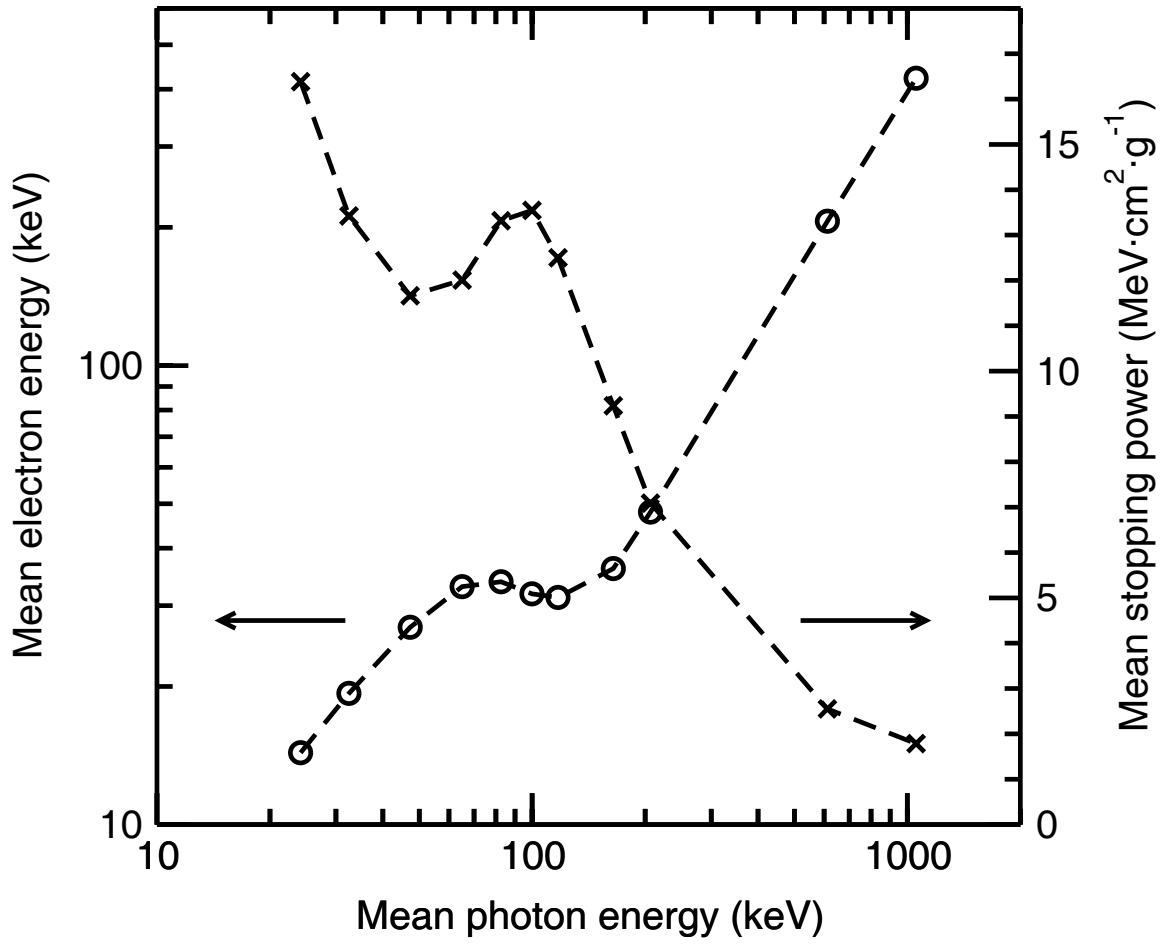

Figure 3.11: Mean electron energy and $\bar{L}/\rho_{\text{coll}}$ as a function of the mean photon energy of the incident beams.

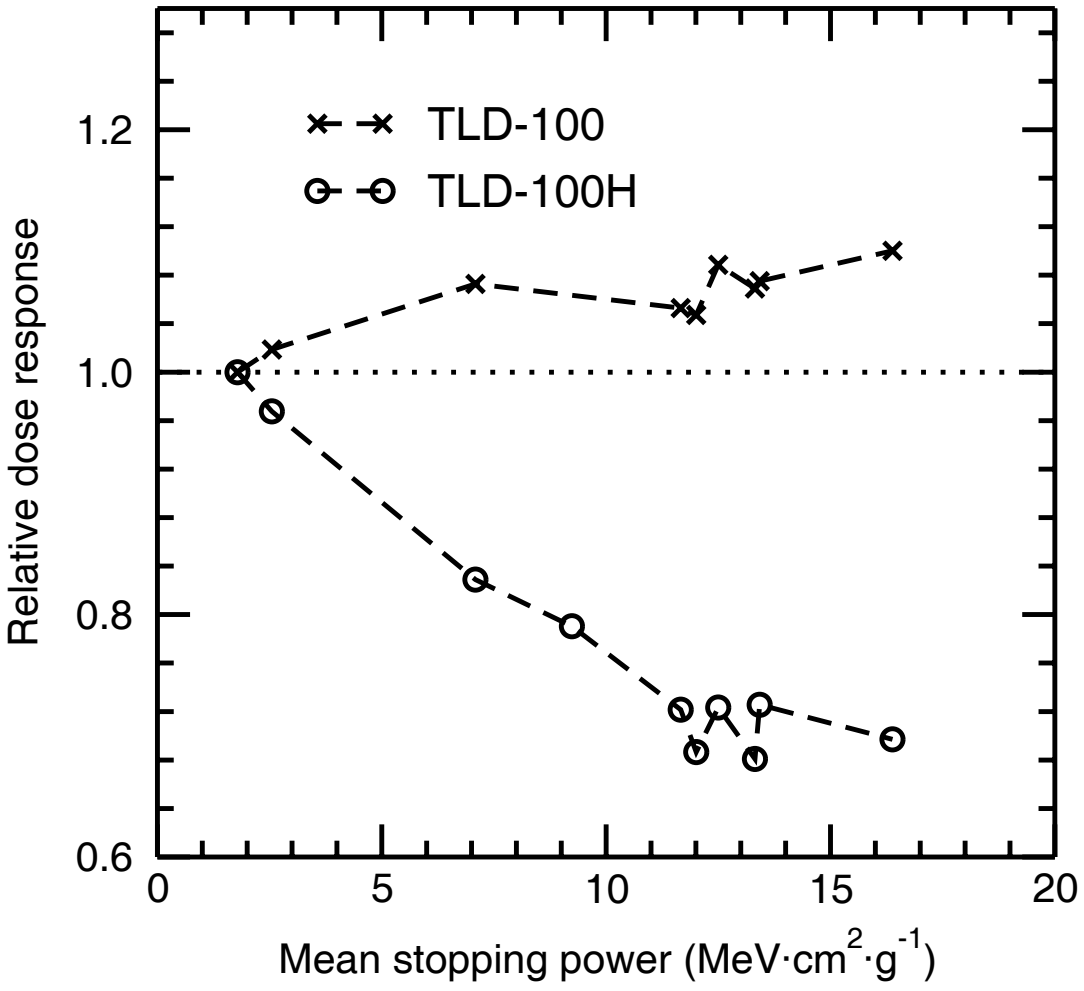

Figure 3.12: Dose response as a function of $\bar{L}/\rho_{\text{coll}}$ for TLD-100 and TLD-100H.

3.5 Conclusions

The TLD-100 energy response measurements were in broad agreement with other published data, but the high level of precision allowed for the observation of the correlation of the response with ionization density. The TLD-100 results were in disagreement with the view in brachytherapy that the intrinsic response is independent of beam quality, and further studies should be conducted to examine the implication of this result for low energy brachytherapy sources.

The TLD-100H results were in good agreement with Olko *et al*, even though the dopant concentrations in MCP-N are quite different from TLD-100H. The Monte Carlo dose calculation was effective in extracting the dose response, but was not able to show an exact relationship between the dose response and the LET of the beam, estimated using the mean restricted mass collision stopping power of electrons in the TLD. Calculations using a microdosimetric Monte Carlo code may be necessary to demonstrate a clear relationship between the dose response and the ionization density.

Chapter 4

Energy Response for Harshaw Type 8855 Environmental Dosimeter

4.1 Introduction

As part of a larger project to characterize the Harshaw Type 8855 environmental dosimeter, the photon energy response was measured for perpendicular irradiations for a number of beam qualities. In this chapter, the energy response results are presented, as well as the residual signal subtraction method implemented to improve the performance at low doses.

4.2 Materials and Methods

4.2.1 TLD specifications

The Harshaw Type 8855 environmental dosimeter (Perry *et al* 1999, Bicron RMP 1999) uses four card-mounted TLD-100H chips with density thickness of 94 $mg \cdot cm^{-2}$. The chips are geometrically identical to the ones used in Chapter 2, but are encapsulated in Teflon® and mounted on aluminium cards. To be used as an environmental dosimeter, the cards are placed in holders with different filters placed over each of the four chips. Element 1 has a 91 $mg \cdot cm^{-2}$ copper filter as well as 240 $mg \cdot cm^{-2}$ of ABS plastic, Element 2 has 100 $mg \cdot cm^{-2}$ of ABS and 930 $mg \cdot cm^{-2}$ of Teflon® in front of the TLD, Element 3 has a thin Mylar® window for a total thickness of 17 $mg \cdot cm^{-2}$, and Element 4 has a 463 $mg \cdot cm^{-2}$ tin filter as well as 240 $mg \cdot cm^{-2}$ of ABS plastic. The filter over Element 2 is hemispherical in shape, while the other filters are flat and circular. The different filters allow for photon energy discrimination, and Element 3 (Mylar® window) can be used to measure the shallow dose from beta particles.

4.2.2 Time-temperature profile and glow curve analysis

The readouts were performed using a Harshaw TLD Model 6600 reader (Bicron RMP 1995), which uses hot nitrogen gas to heat the TLDs. The 6600 reader has two separate photomultiplier tubes (PMTs), so that two chips on the card can be read simultaneously. The temperature of the chips is controlled by two separate thermocouples mounted between the gas jets and the chips. Unlike the bare chips, no ovens were used to preheat or anneal the card-mounted chips, and both of these processes were performed, to some extent, during the readout. The readout consisted of a preheat at 165°C for 10 seconds, during which the PMT signal was not recorded. Immediately

following the preheat, the temperature was increased linearly at 15°C·s^{-1} up to a maximum temperature of 260°C, where the temperature was held constant. The PMT signal was recorded during the linear heating phase and at the maximum temperature, for a total acquisition time of 16 2/3 seconds. The 260°C temperature was maintained for an additional 10 seconds after the signal acquisition, to anneal some of the residual signal from the TLDs. The time-temperature profile (TTP) was specified based on the temperature of the thermocouples, so the actual temperature of the chips would be expected to be somewhat less than predicted by the TTP due to thermal lag.

The signal recorded during the acquisition period was stored in 200 data channels, and typical glow curves are shown in Figure 4.1. The NETREMS software accompanying the reader was only used to control the reader and store the glow curves, and was not used to generate reader calibration factors (RCFs) or element correction coefficients (ECCs). The data analysis was performed independently using a Microsoft Access® database.

In comparison with the bare chip reader, the glow curves from the hot gas reader demonstrated a higher signal in the low temperature region, due to the relatively short preheat time (cf. Figure 2.3). The signal in the low temperature region was proportional to the height of the main glow peak, although the proportionality changed slightly depending on the fading time. In contrast, at low doses the signal in the high-temperature tail was almost entirely dependent on the dose history of the TLD, and was due to residual signal left from earlier irradiations. The cards were not oven-annealed, so the only way to reduce the residual signal was by re-reading the card in the 6600 reader. The cards were re-read using the standard TTP, and a typical re-read signal is shown in Figure 4.2. The integral signal from a re-read TLD was approximately 1% of the signal from the original reading, and the signal from a third reading was approximately 0.3% of the original signal.

The residual signal in LiF:Mg,Cu,P was originally seen as one of the major drawbacks of the material, with reports of a total residual signal of 7% (Horowitz and Horowitz 1990), and helped prevent its widespread acceptance in earlier formulations. The residual signal arises from glow peaks at about 270°C and 295°C, which cannot be fully read out without a subsequent loss of sensitivity in the TLD (Bacci *et al* 1993). The recommended maximum temperature for

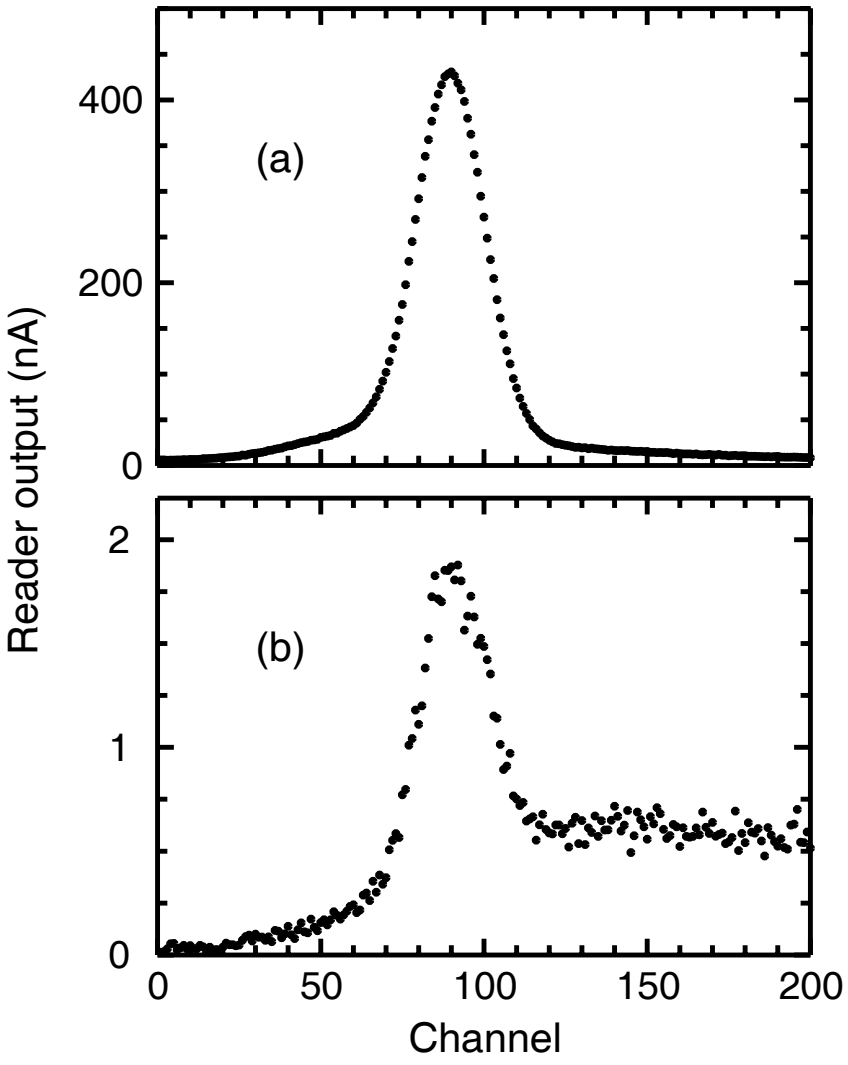

Figure 4.1: Typical glow curves for TLD-100H using the Harshaw Model 6600 hot gas reader. The curve shown in (a) was from a delivered air kerma of 2 mGy, and the curve shown in (b) was from environmental background radiation over 48 hours (~6 μGy).

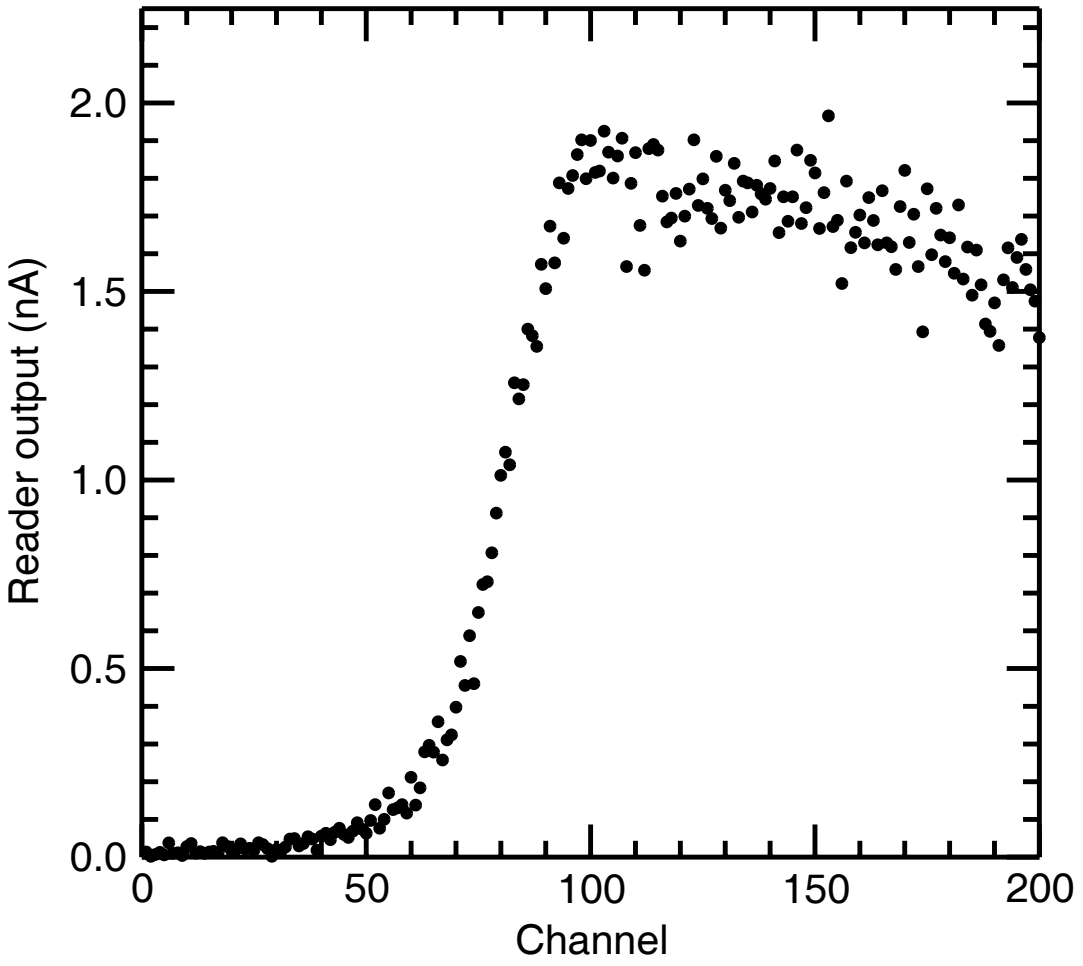

Figure 4.2: Typical re-read signal after a delivered air kerma of 2 mGy.

LiF:Mg,Cu,P is generally 240°C ± 5°C to avoid a loss in sensitivity, but several authors have found that this limit can be exceeded for brief periods with little or no change in sensitivity (Gómez Ros *et al* 1996, Oster *et al* 1996). Although the maximum temperature for the TTP used in this work was 260°C, it is unclear what temperature the chips actually reached during the readout cycle.

Moscovitch (1999) has suggested using multiple re-reads to reduce the residual signal in unannealed LiF:Mg,Cu,P, and Delgado *et al* (1995) have suggested a method to subtract the contribution of the residual signal. A combination of these approaches was taken for this work, in order to be able to use the TLDs for the low doses encountered in environmental dosimetry. The TLDs used for the energy response measurements received high enough doses so that the residual signal contribution was very small, but since the system was eventually intended for environmental applications the residual signal needed to be addressed.

Several simple subtraction methods were attempted using the region-of-interest (ROI) settings available with the 6600 reader, but it was found that the chip-to-chip variability with respect to glow curve structure and peak positions made any universal methods ineffective. Another attempt used the signal from a re-read TLD to determine the amount of residual signal present in the original glow curve, but this method also proved ineffective. The amount of residual signal present in a re-read TLD varied slightly depending on the TLD element, since the two gas jets and thermocouples in the 6600 reader could not be calibrated to heat the two sets of chips in exactly the same way. In addition, the position of the TLDs in the Teflon® encapsulation with respect to the gas jets was not identical for every card, and the resulting small differences in the chip temperatures lead to measurable differences in the fraction of remaining residual signal.

Fortunately, the glow curve structure for any given chip was remarkably consistent over a series of readout cycles, and a subtraction method using the individual glow curve structure proved quite reliable. The subtraction algorithm was based on the method published by Delgado *et al*, which they used for LiF:Mg,Cu,P bare chips and a planchet-type reader. The algorithm was implemented in the Microsoft Access® database, and was used to automatically determine the net signal for every glow curve. The simple glow curve analysis was easier to implement than

traditional glow curve deconvolution methods, and required essentially no user intervention. Several modifications were made to the method of Delgado *et al*, and a complete description of the algorithm is provided below.

4.2.2.1 Outlier detection and removal

The glow curves resulting from low doses contained much more noise than glow curves from higher doses, as expected, but in some cases there were single-channel spikes in the glow curve that were much higher than the background noise. These outliers were not observed for the planchet-type reader, but were occasionally observed for the hot gas reader, with large spikes appearing in about 1% of the glow curves. It has been suggested that these spikes could be due to spontaneous TL from foreign contaminants in the gas, but a conclusive explanation is not known.

Most glow curve analysis algorithms use some form of outlier removal, and two complementary methods were implemented here. The first method was suggested by Gaulke[1], and identified an outlier by comparing the signal in a given channel, i, to the signals in the channels from i-4 to i+4. The nine channels were ranked in order, with the lowest ranked signal denoted $S_{\min}$ and the seventh ranked signal denoted S_{med}. If the signal in channel i, S_i, was ranked eighth or ninth then it was considered an outlier if

$$\frac{S_i - S_{\min}}{S_{\text{med}} - S_{\min}} \geq 4\,, \tag{4.1}$$

which roughly corresponded to more than four standard deviations away from the mean. If S_i was deemed an outlier, the signal was replaced with the mean value from the first to seventh ranked signals. This method was effective in removing up to two outliers in any nine-channel window in the glow curve, and was modified slightly so that it would also work near the ends of the glow curve.

It was found that Gaulke's method could fail for outliers on the sides of the glow peak, where the signal changed very rapidly and the difference between S_{med} and $S_{\min}$ could be quite large. To

[1] Gaulke, B. (Health Canada) Private communication.

deal with outliers in this region, a second outlier detection algorithm was also used, based on the method implemented by Figel and Sprunck (1999). A Savitzky-Golay smoothing filter was applied to the raw data, and once again, an outlier was identified by comparing the signal in a given channel, *i*, to the signals in the channels from *i*-4 to *i*+4. Calculated squared differences between the smoothed data and the raw data were averaged from *i*-4 to *i*+4, excluding channel *i*. The average squared difference, denoted $<s^2>$, was compared with the squared difference between the smoothed data and the raw data in channel *i*, denoted *d*. The signal in channel *i*, S_i, was deemed an outlier if

$$\frac{d}{< s^2 >} \geq 36 , \tag{4.2}$$

and S_i was higher than the smoothed signal. This corresponded to roughly six standard deviations away from the smoothed signal. If S_i was deemed an outlier, the signal was replaced with the smoothed value. This method only removed the positive outliers associated with the hot gas reader, and did not work in instances where two outliers were within four channels of each other. These so-called "double spikes" were very rare, and were removed if they occurred outside the peak region using Gaulke's method.

An example glow curve is presented in Figure 4.3, with several outlier data points manually added to the original glow curve to test the effectiveness of the outlier detection algorithms. The number of outliers is greatly exaggerated, since the likelihood of even a single outlier for this level of signal was typically about 1%.

4.2.2.2 Savitzky-Golay smoothing and characteristic feature detection

The residual signal subtraction algorithm was based on the method published by Delgado *et al*, but was modified for use with the hot gas reader and the TTP used in this work. Once the outliers were removed from the raw signal, the data points were smoothed using a three-pass Savitzky-Golay filter (Press *et al* 1992). The smoothing window was 21 channels wide, and a quadratic smoothing polynomial was selected. The Savitzky-Golay filter did not change the integral under the glow curve, but it was necessary to have a smooth signal to be able to find the characteristic points on the curve.

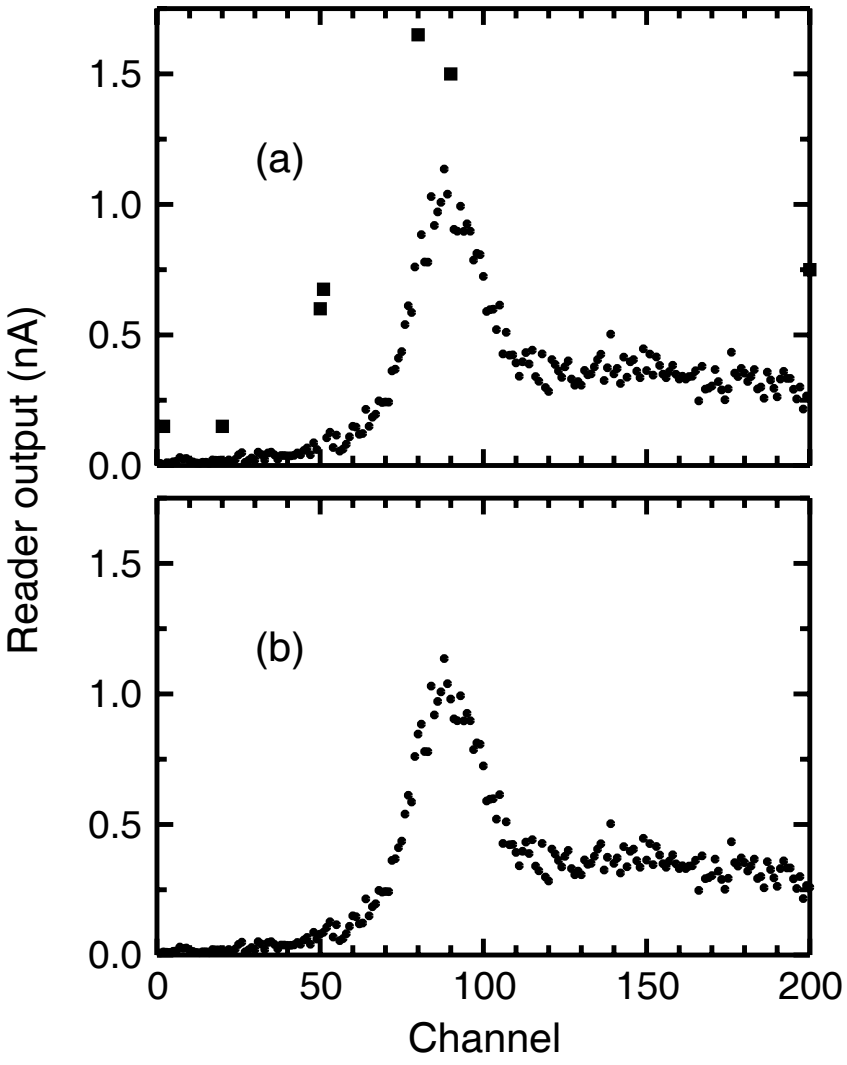

Figure 4.3: (a) Example glow curve with identified outliers marked as squares, and (b) the resulting glow curve with the outliers removed. The original raw data points were manually adjusted to include several outliers, to test the effectiveness of the outlier detection algorithms.

The Savitzky-Golay algorithm was also used to find smoothed first and second derivatives of the smoothed signal, with an example shown in Figure 4.4. The characteristic point n_M was identified as the channel with the minimum value in the second derivative, and corresponded roughly with the peak channel in the glow curve. The local maxima on either side of the global minimum in the second derivative corresponded to points of inflection in the first derivative, and the tangents to the curve at the points of inflection were extrapolated back to the x-axis to determine channels n_L and n_R. Another channel, n_T, was calculated as 1/4 of the distance between channels n_M and n_R. As stated by Delgado *et al*, the methods used to select n_L and n_R appear somewhat artificial, but they roughly corresponded with points on the residual signal curve. The n_T point was not included in the algorithm by Delgado *et al*, but was necessary for the hot gas reader because the peak in the residual signal appeared only slightly later than the maximum signal in the main dosimetric peak. This was likely due to thermal lag effects, and future work could examine this further by modifying the heating rate used in the TTP. The distance between n_M and n_T was empirically derived based on the results from several residual signal experiments.

The subtraction region is shown in Figure 4.5 along with the resulting net glow curve. The subtraction region had a shape similar to the residual signal, but since it did not model the shape of the residual signal precisely, the net glow curve demonstrated a noticeable artefact in the early part of the curve. This artefact was only visible when the subtraction region was a large fraction of the original glow curve. The subtraction method removed the residual signal from earlier exposures by effectively removing the contribution from any glow curve peaks beyond the main dosimetric peak.

4.2.2.3 Residual signal subtraction test

To test the effectiveness of the residual signal subtraction method, five groups of five calibrated cards were exposed to air kerma levels of 0, 0.2, 0.4, 0.7, and 0.9 mGy, and were read once in the 6600 reader. The cards were then used to measure the background environmental exposure over 24 hours, which was approximately 3 μGy. The results are presented in Section 4.3.1.

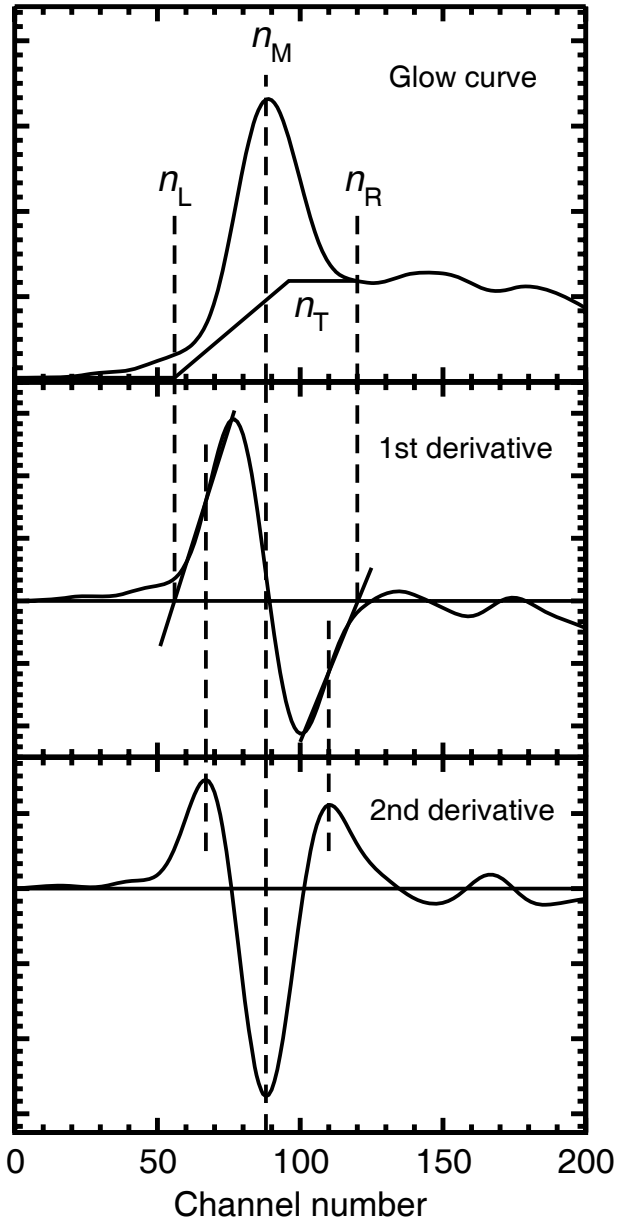

Figure 4.4: Identification of characteristic points in the subtraction algorithm.

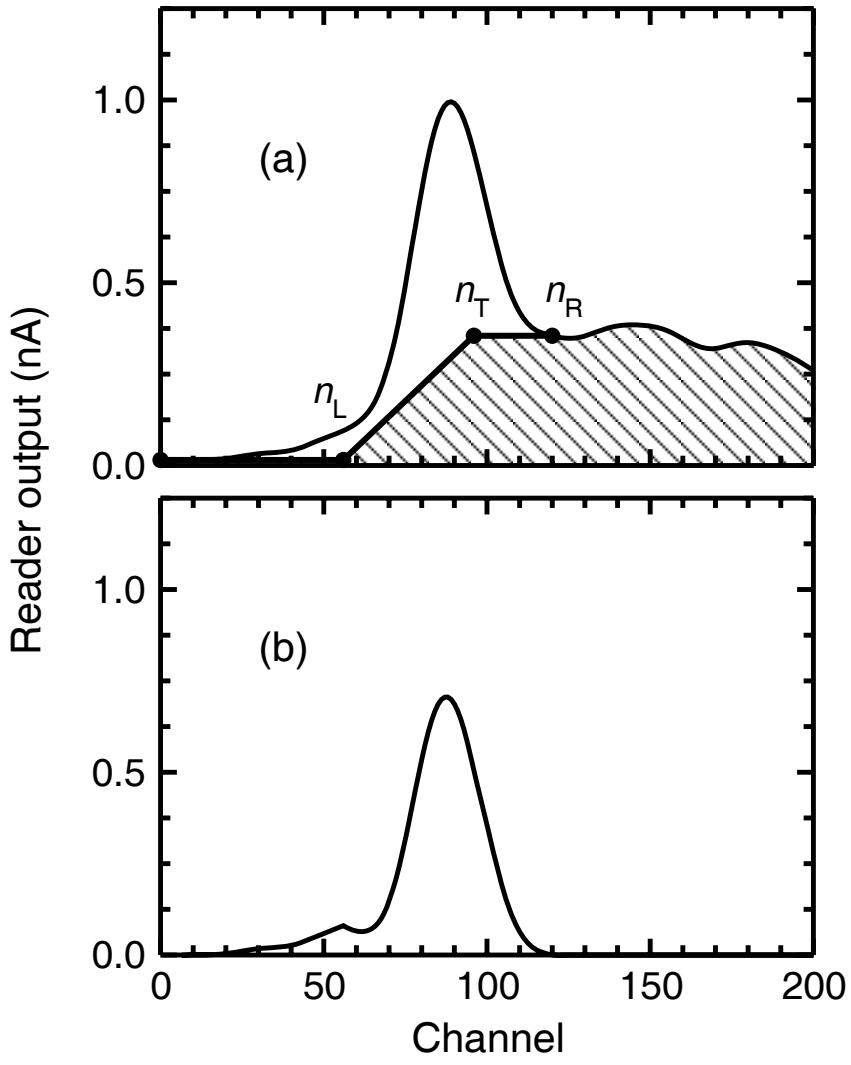

Figure 4.5: (a) Glow curve subtraction region and (b) net glow curve.

4.2.3 Photon energy response measurements

The energy response of the 8855 dosimeter was tested using the same photon beams as in Chapter 2, namely the ISO narrow spectrum series x-ray beams from 30 kV to 250 kV, as well as the ^{137}Cs and ^{60}Co sources. The irradiations were performed using single holders in a free-in-air geometry, with the holders suspended in air at the reference distance from the source using two thin aluminium wires attached to a rotating steel frame. Two perpendicular telescopes were used to align the centre of the holder at the reference point of the beam. The estimated uncertainty on the positioning of the holder was 0.5 mm in the direction of the beam, and 1.0 mm perpendicular to the beam.

The TLDs were calibrated in the ^{60}Co beam by irradiating the bare cards in a PMMA phantom with front and back wall thicknesses of 5.8 mm. The cards were irradiated to an air kerma level of 2 mGy at 3 m from the ^{60}Co source, and up to 12 cards could be irradiated simultaneously. The cards were divided into groups of five, with one group used to measure the background environmental exposure, and one group used as reference cards. The reference cards were irradiated in the ^{60}Co beam in the PMMA phantom, and were used to correct for any changes in the reader calibration. All of the other cards were irradiated in holders in the test beam. As part of the broader study of the angular response of the 8855 dosimeter, groups of five cards were irradiated at several different angles. Five separate holders were used for most of the irradiations, but only a single holder was used for the ^{137}Cs, N-150, and N-250 test beams. The time between the calibration of the cards and the experimental readouts was typically less than 5 days.

Similar to the bare chip work presented in Chapter 2, the air kerma at the point of reference was accurately known for each of the test beams, and the measured air kerma was determined using the measured net TL signal and the ^{60}Co calibration factor. The measured air kerma was divided by the known delivered air kerma to determine the air kerma response.

4.2.4 Monte Carlo simulations of the 8855 dosimeter

Monte Carlo simulations were performed for three of the elements in the 8855 dosimeter, to compare the calculated energy response to the measured energy response. As with the bare chip calculations, the geometry was simplified to have cylindrical symmetry, and the user code DOSRZnrc was used for the simulations. Elements 1 (copper filter), 3 (Mylar® window), and 4 (tin filter) were modelled as separate cylinders, and scattered photons from other parts of the dosimeter were not taken into consideration. Element 2 (Teflon®) was not simulated because the hemispherical filter could not be modelled easily using the DOSRZnrc user code. The filter thicknesses were obtained from Perry *et al* (1999), and the thickness of the Teflon® encapsulation was obtained from King and Cassata (2000). All of the other holder dimensions were determined by dismantling one of the holders, and a micrometer was used to measure the individual components. Air gaps were estimated based on the measurements of the individual components compared with measurements of the assembled holder.

The copper and tin filters, and the aluminium in the cards, were considered to have no impurities, so the materials used in the simulations were generated using the pure elements. The Teflon® encapsulation material was modelled as pure polytetrafluoroethylene (C_2F_4), and the Mylar® window on Element 3 was modelled as pure polyethylene terephthalate ($C_{10}H_8O_4$). Density correction information for the Teflon® and Mylar® materials was available with the EGSnrc distribution. The ABS resin used in the holder was a mixture of acrylonitrile (C_3H_3N), butadiene (C_4H_6), and styrene (C_8H_8). Different ABS resins use different proportions of the components based on the desired material characteristics, but the specific mixture used in the 8855 dosimeter was not available. A generic mixture of 30% acrylonitrile, 20% butadiene, and 50% styrene was used to generate the ABS material. The air and TLD-100H materials were the same as those used in Chapter 3.

The DOSRZnrc simulations were used to calculate the dose to the TLD per unit of incident fluence, and the air kerma per unit fluence calculations from Chapter 3 using the same photon beams were used to determine the dose per unit air kerma. The EGSnrc transport parameters were the same as for the bare chips, with cutoffs of 1 keV for photons and 10 keV for electrons.

Some extra simulations were also performed with a cutoff of 1 keV for electrons to ensure that the choice of cutoff was not too high.

4.3 Results and Discussion

4.3.1 Residual signal subtraction algorithm

The measured background using the subtraction algorithm was compared to the measurements using conventional analysis, with the results for Element 2 shown in Figure 4.6. The conventional analysis used a simple integral of the glow curve from channels 1 to 160 to determine the measured air kerma. As can be seen in Figure 4.7, if a relatively large residual signal is left on the TLD, a simple integral would not be effective, and some kind of subtraction method would be necessary to be able to measure low doses accurately.

The subtraction algorithm performed well for the residual signal levels in the experiment, with an overall relative standard deviation of 7% for the measured background of 2.7 μGy, using the results for all four elements and at all of the residual signal levels. In practice, cards were usually re-read at least once after irradiations above 1 mGy, to reduce the amount of residual signal and to allow for less reliance on the subtraction method. At low levels of residual signal, the detection limit achievable using this method was less than 1 μGy.

4.3.2 Photon energy response results

The results of the photon energy response measurements are presented in Table 4.1, relative to the ^{60}Co calibration in the PMMA phantom. The results are also presented in Figure 4.8, with the results normalized to the ^{60}Co response for each element.

The results were in fairly good agreement with data from SGC&D[1], which were generated using different x-ray qualities than the ones used in this work, with their results shown in

[1] Luo, L. Z. (SGC&D) Private communication.

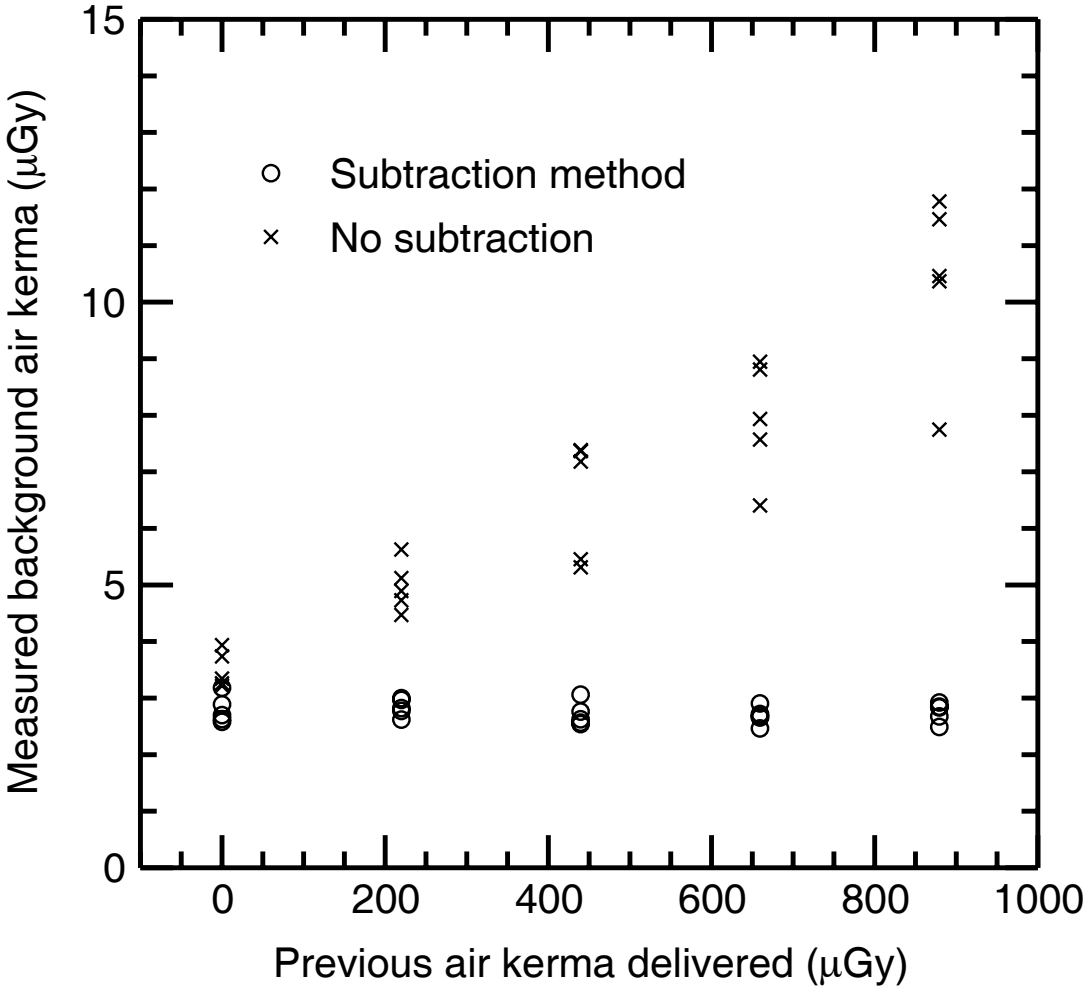

Figure 4.6: Measured background as a function of the previous air kerma delivered to the card.

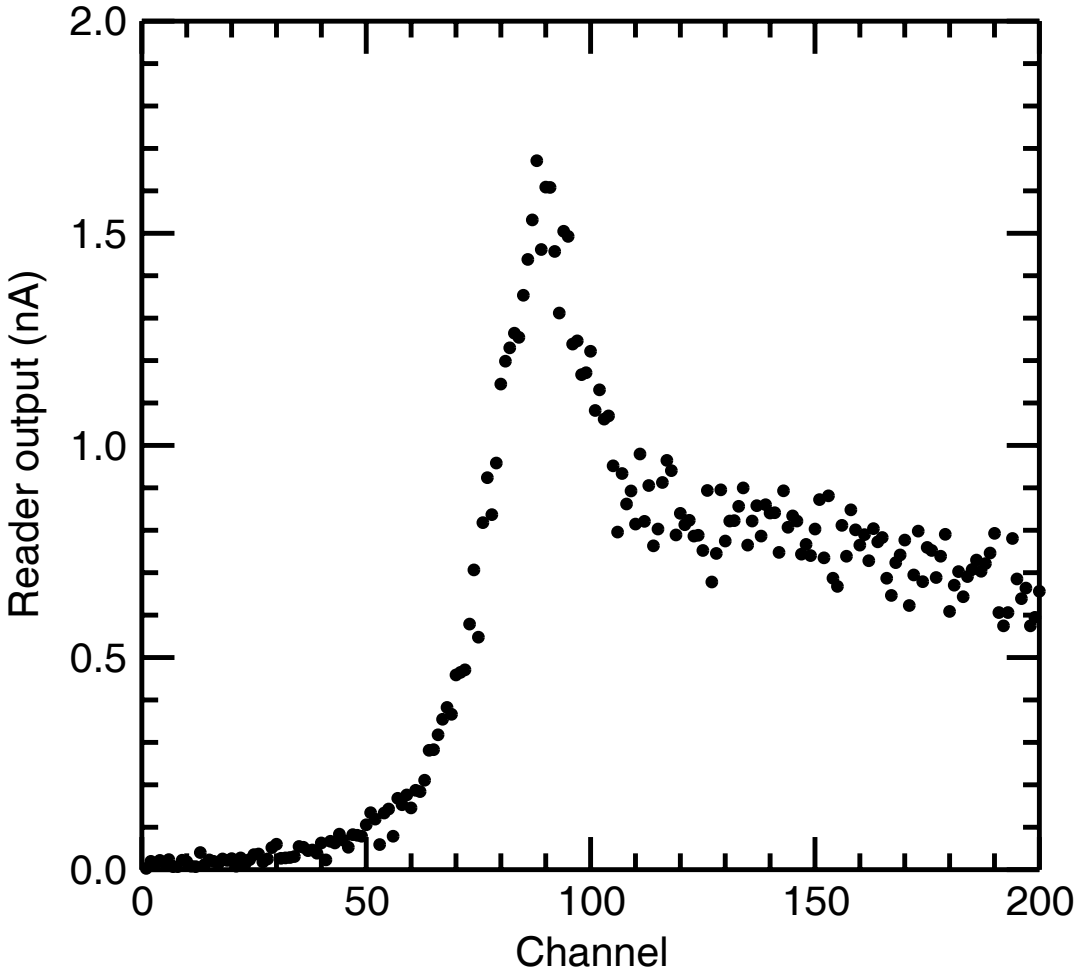

Figure 4.7: Glow curve from environmental background of ~3 μGy for a TLD with residual signal from a 900 μGy irradiation.

Photon beam	Mean energy (keV)	Element 1 (copper)	Element 2 (Teflon®)	Element 3 (Mylar®)	Element 4 (tin)
N-30	24	0.222	0.624	0.970	0.024
N-40	32	0.550	0.827	1.007	0.041
N-60	47	0.850	0.910	0.991	0.080
N-80	65	0.855	0.826	0.875	0.218
N-100	83	0.803	0.756	0.796	0.379
N-150	117	0.806	0.755	0.795	0.593
N-200	164	0.871	0.792	0.825	0.826
N-250	207	0.911	0.815	0.852	0.983
^{137}Cs	612	0.957	0.927	0.938	1.096
^{60}Co	1055	0.997	0.966	0.770	1.020

Table 4.1: Air kerma response for the 8855 dosimeter, relative to the ^{60}Co calibration in the PMMA phantom. The uncertainties range from 0.4% at the high energies to 5% at the low energies.

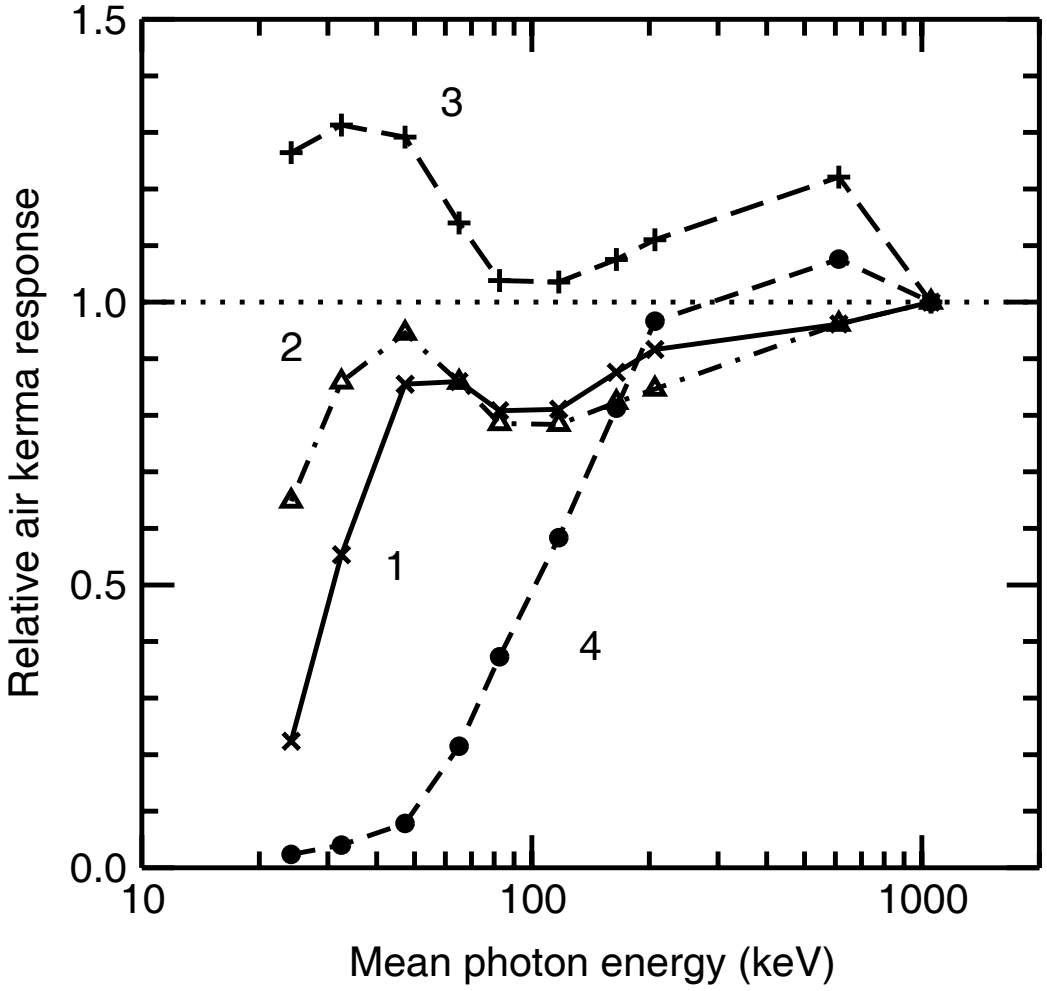

Figure 4.8: Air kerma response measurements for the 8855 dosimeter, normalized to the ^{60}Co results. The curves are numbered corresponding to each element: 1 – copper filter, 2 – Teflon®, 3 – Mylar® window, 4 – tin filter.

Figure 4.9. An exception was the Element 3 result for the ^{60}Co beam, with an 18% under-response relative to the ^{137}Cs response compared with the SGC&D results. The ^{60}Co irradiations for the SGC&D measurements were performed with a sheet of PMMA in front of the holder to provide charged particle equilibrium for each of the four elements, while the irradiations performed at the NRC used a free-in-air geometry for all of the test beams. Element 3 was covered with only a very thin Mylar® window, so there was a lack of charged particle equilibrium for the ^{60}Co irradiations, resulting in an under-response relative to the other photon beams.

4.3.3 Monte Carlo simulation results

The DOSRZnrc simulations were used to calculate the dose to the TLD per unit air kerma for Elements 1, 3, and 4. It was known from the bare chip measurements and calculations in Chapters 2 and 3 that the response of TLD-100H strongly depended on the ionization density of the photon beam, so the calculated doses for each photon beam were multiplied by the TLD-100H energy response determined in Chapter 3. This assumed that the ionization density of each of the photon beams was the same in the 8855 holder as in the PMMA phantom used for the bare chips, even though the tin and copper filters would likely have an effect on the photon spectrum at the TLD. It also assumed that the differences in readout protocols between the planchet-type reader and the hot gas reader did not have an effect on the energy response, although other reported results show that this assumption may not be true (Horowitz 1993). The dose calculations for Elements 1 and 4, normalized to the ^{60}Co result, are presented in Figure 4.10. The Monte Carlo calculated values are within 5% of the measurements for photon energies above 60 keV, with some larger discrepancies at energies below 60 keV. The discrepancies between the measured and calculated values at the lower energies are up to 10%, which may be because the calculations are much more sensitive to the exact thickness of the filters for the low photon energies. In addition, the measurement uncertainties are up to 5% for the lowest photon energies. There was no statistical difference for the simulations performed with an electron kinetic energy cutoff of 1 keV.

The Monte Carlo calculations for Element 3 were not accurate for the ^{137}Cs and ^{60}Co beams due to the lack of build-up material covering the chip. The Monte Carlo simulations did not take

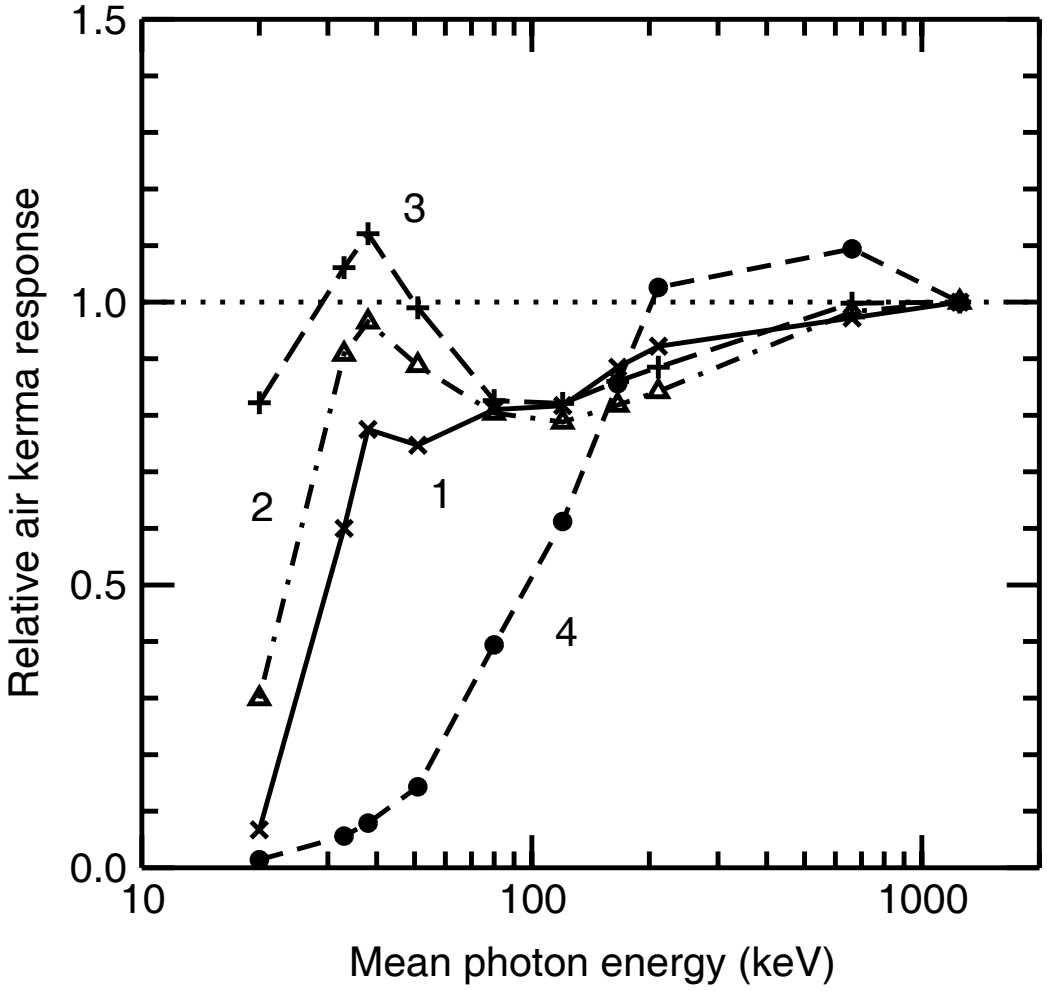

Figure 4.9: Air kerma response measurements for the 8855 dosimeter conducted by SGC&D, normalized to the ^{60}Co results. The curves are numbered corresponding to each element: 1 – copper filter, 2 – Teflon®, 3 – Mylar® window, 4 – tin filter.

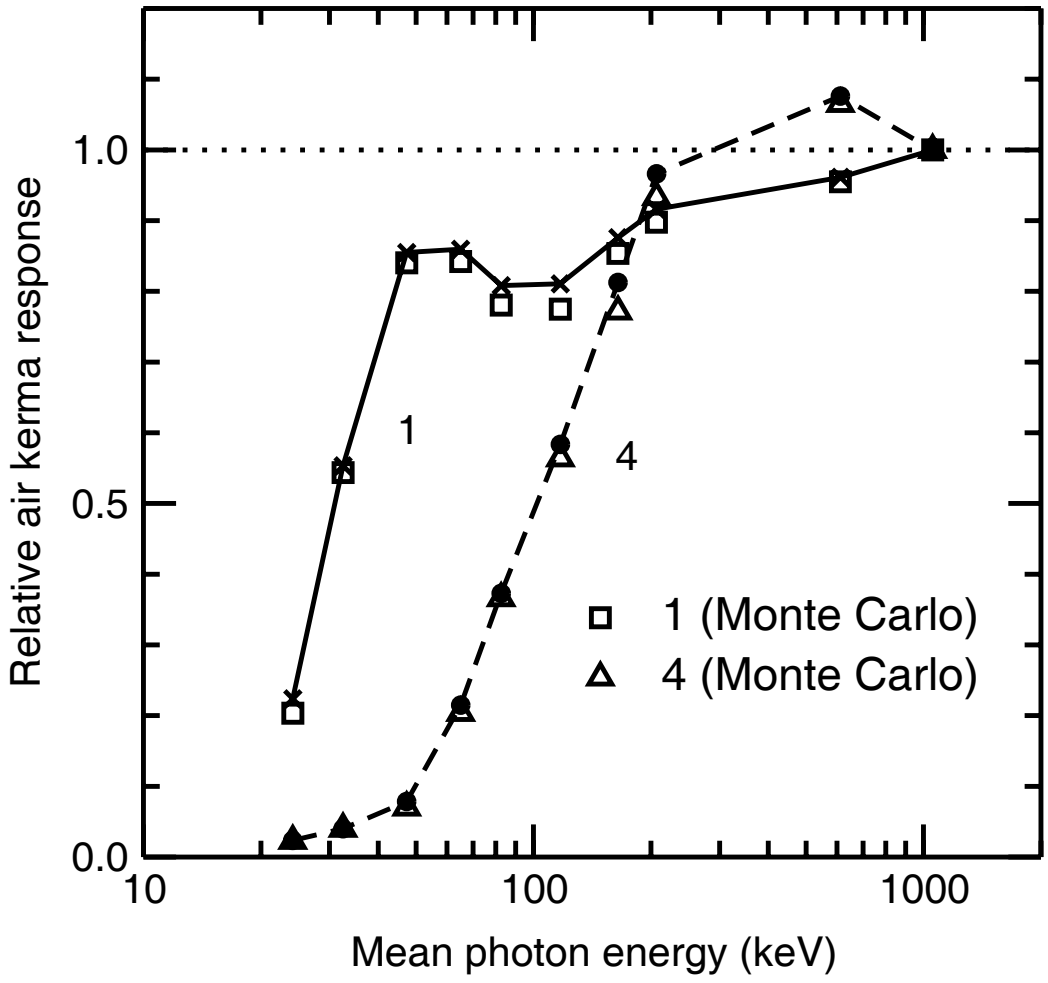

Figure 4.10: Monte Carlo calculated energy response in the 8855 dosimeter for Elements 1 (copper) and 4 (tin).

into account electron contamination in the photon beams, so the calculated doses were much lower than the measured values for the higher energy beams. This problem did not occur for the x-ray beams, so by normalizing the Monte Carlo calculated results to the measurements for the N-250 beam, it was possible to compare the calculations to the measurements for all of the ISO series x-ray beams. The results for Element 3 are presented in Figure 4.11, and the agreement between the calculated and measured results is within 3% for all of the x-ray beams. The ^{137}Cs calculation is also shown, with a calculated result 24% lower than the measurement.

4.4 Conclusions

The energy response measurements were in broad agreement with the results from SGC&D, except for Element 3 (Mylar®), which under-responded relative to the SGC&D results. This was due to the lack of build-up material used for the irradiations at the NRC, which should not normally be used when measuring the energy response of a dosimeter if it is intended to be used in the field without any build-up material.

The Monte Carlo calculations were in good agreement with the measured results, which suggests that Monte Carlo techniques could prove useful for future dosimeter designs. It may also be possible to use Monte Carlo techniques to model the angular response of the dosimeter as well, but this would require much more detailed measurements and a fairly complicated model for the simulations.

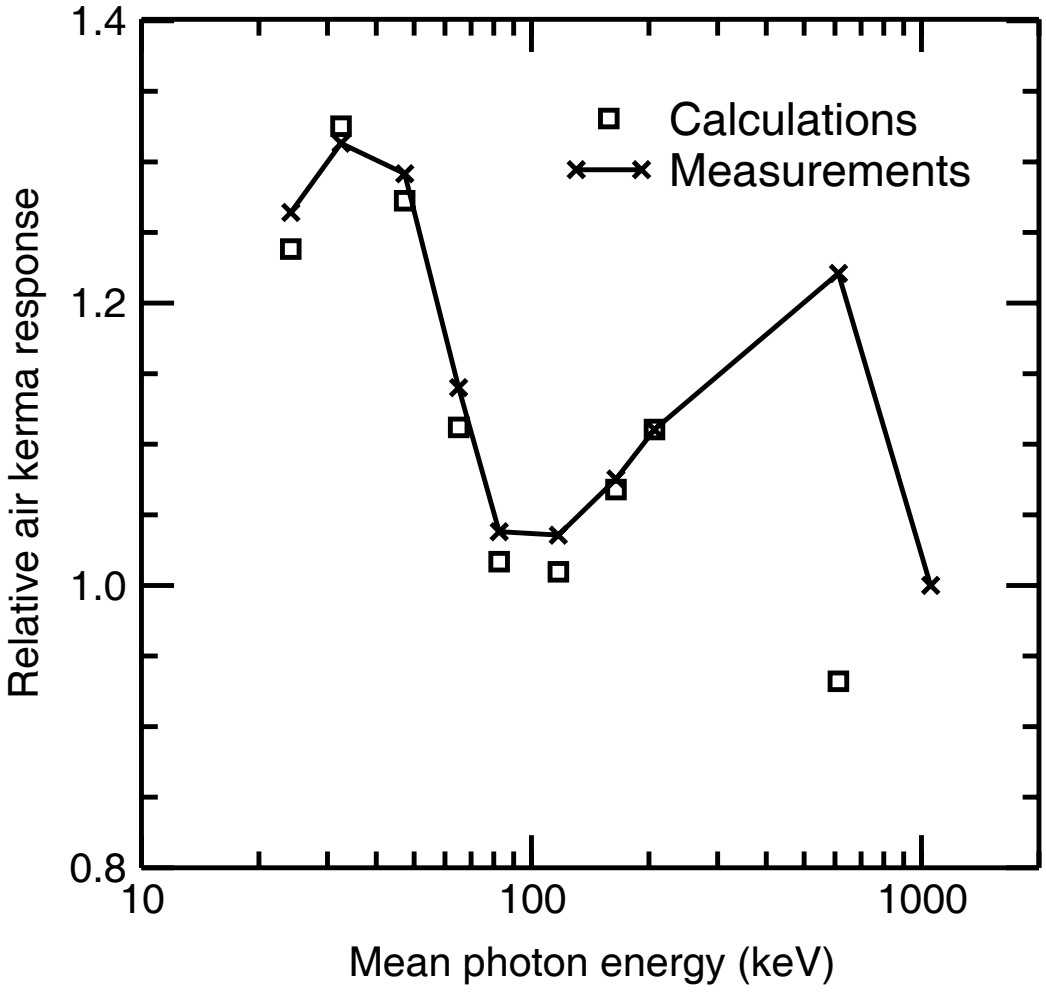

Figure 4.11: Monte Carlo calculated energy response in the 8855 dosimeter for Element 3 (Mylar® window).

Chapter 5

Summary and Conclusions

5.1 Summary of Results

5.1.1 Chapter 2: Bare Chip Energy Response Measurements

Chapter 2 describes the air kerma response measurements for TLD-100 and TLD-100H, with some details of the annealing, readout, and calibration protocols employed. A non-linearity with respect to the delivered air kerma is noted for the Victoreen 2800M reader, and it is suspected that it was an artefact of the reader, so the results are corrected for the measured non-linearity. The air kerma response measurements are in broad agreement with other published data for TLD-100 and TLD-100H, although the precision of the results is better than most of the other published data.

5.1.2 Chapter 3: Bare Chip Monte Carlo Calculations

Chapter 3 details the Monte Carlo simulations of the TLD holder using EGSnrc, to calculate the absorbed dose to the TLDs for the measurements described in Chapter 2. The TLD dose response is calculated as a function of mean photon energy for both TLD-100 and TLD-100H, and the results are in agreement with other published data. The implications of the TLD-100 response are discussed with respect to applications in brachytherapy, with a potential for calibration errors of up to 10% for ^{125}I and ^{103}Pd brachytherapy sources. Although the reason for this discrepancy is unclear, there is a need for further investigation in this area. The TLD-100H dose response is compared with the results of Olko *et al* (1993), and the correlation of the dose response with the ionization density of the photon beams is demonstrated.

5.1.3 Chapter 4: Energy Response for Harshaw Type 8855 Environmental Dosimeter

Chapter 4 describes the use of the Harshaw TLD Model 6600 reader with card-mounted TLD-100H, and explains the residual signal subtraction method used to improve the dosimeter performance at low doses. The photon energy response measurements are in broad agreement with the data from SGC&D. The lack of build-up material for the ^{60}Co irradiations led to a

substantial difference between the present measurements and the data from SGC&D for Element 3 (Mylar® window). The results from EGSnrc Monte Carlo simulations of three of the dosimeter elements are presented, and the calculations are generally within 5% of the measured results.

5.2 Future Work and Conclusions

The photon energy response results broadly agreed with existing data, but there is much more work that could be performed. The photon energy response measurements of the bare chips could be extended to lower and higher energy photons than those used in this work, although at low energies the Monte Carlo calculations would need a very accurate photon spectrum as a source input. Other properties of the TLD material, such as fading and light sensitivity should also be looked at in more detail.

Measurements have already been performed for the angular dependence of the 8855 dosimeter, and an attempt could be made to simulate the entire dosimeter in three-dimensions and compare the calculations with the angular response measurements.

There are also many other aspects of the 8855 dosimeter to be examined pertaining to environmental dosimetry. The ratios of the responses from the separate elements are used to calculate the relevant dose equivalent quantities for environmental dosimetry, and these methods need to be evaluated to determine whether the 8855 dosimeter is a suitable environmental dosimeter. LiF:Mg,Cu,P looks to be a promising material for use in environmental and personnel dosimetry, but more work is necessary to characterize the phosphor fully.

Bibliography

Attix F H 1986 *Introduction to Radiological Physics and Radiation Dosimetry* (New York, NY: John Wiley & Sons)

Bacci C, D'Angelo L, Furetta C and Giancola S 1993 Comprehensive study on LiF:Cu,Mg,P (GR-200 A) *Radiat. Prot. Dosim.* **47** 215-218

Berger M J, Hubbell J H, Seltzer S M, Coursey J S and Zucker D S 1999 *XCOM: Photon Cross Section Database* (version 1.2) http://physics.nist.gov/xcom (Gaithersburg, MD: National Institute of Standards and Technology)

Bicron Radiation Measurement Products 1995 *Model 6600/6600E Automatic TLD Workstation Operator's Manual* Pub. No. 6600-E-O-0395-001 (Solon, OH: Saint-Gobain Industrial Ceramics Corporation)

Bicron Radiation Measurement Products 1999 *Dose Calculation Algorithm for the Type 885X Environmental Dosemeter - User's Manual* ALGM-EH-U-0199-003 (Solon, OH: Saint-Gobain Industrial Ceramics, Inc.)

Bielajew A F and Rogers D W O 1987 PRESTA: the parameter reduced electron-step transport algorithm for electron Monte Carlo transport *Nucl. Instrum. Methods* B **18** 165-181

Bielajew A F, Hirayama H, Nelson W R and Rogers D W O 1994 *History, Overview and Recent Improvements of EGS4* NRC Report PIRS-0436 (Ottawa, ON: National Research Council Canada)

Borg J, Kawrakow I, Rogers D W O and Seuntjens J P 2000 Monte Carlo study of correction factors for Spencer-Attix cavity theory at photon energies at or above 100 keV *Med. Phys.* **27** 1804-1813

Budd T, Marshall M, Peaple L H J and Douglas J A 1979 The low- and high-temperature response of lithium fluoride dosemeters to x-rays *Phys. Med. Biol.* **24** 71-80

Burlin T E 1966 A general cavity theory of ionization *Br. J. Radiol.* **39** 727-734

Cameron J R 1970 *Nine year review of thermoluminescence dosimetry research at the University of Wisconsin 1961 - 1970* COO-1105-154 (Madison, WI: University of Wisconsin)

Cusimano J P, Cipperley F V and Culley J C 1968 *Special applications of thermoluminescence dosimetry* IDO-12068 (Idaho Falls, ID: United States Atomic Energy Commission)

Da-Ke W, Fu-Yin S and Hong-Chen D 1984 A high sensitivity LiF thermoluminescent dosimeter - LiF(Mg, Cu, P) *Health Phys.* **46** 1063-1067

Das R K, Li Z, Perera H and Williamson J F 1996 Accuracy of Monte Carlo photon transport simulation in characterizing brachytherapy dosimeter energy-response artefacts *Phys. Med. Biol.* **41** 995-1006

Delgado A, Gómez Ros J M and Muńiz J L 1995 Computerised analysis of LiF GR-200 TL signals: application to dose measurements in the μGy range *Radiat. Prot. Dosim.* **60** 147-153

Figel M and Sprunck M 1999 Fast cooling and computerised glow curve deconvolution in routine personnel monitoring with TLD-100 *Radiat. Prot. Dosim.* **81** 259-264

Ford R L and Nelson W R 1978 *The EGS Code System: Computer Programs for the Monte Carlo Simulation of Electromagnetic Cascade Showers (Version 3)* SLAC-210 (Stanford, CA: Stanford Linear Accelerator Center)

Frujinoiu C 2001 Reconsideration of the backscatter components in the intermediate cavity theory for photon beams *Phys. Med. Biol.* **46** 1205-1217

Gamboa-deBuen I, Buenfil A E, Ruiz C G, Rodríguez-Villafuerte M, Flores A and Brandan M E 1998 Thermoluminescent response and relative efficiency of TLD-100 exposed to low-energy x-rays *Phys. Med. Biol.* **43** 2073-2083

Gómez Ros J M, van der Burg B, Muńiz J L and Delgado A 1996 Glow curve control of the maximum readout temperature: application to LiF GR-200 *Radiat. Prot. Dosim.* **66** 423-426

Haider J A, Skarsgard L D and Lam G K Y 1997 A general cavity theory *Phys. Med. Biol.* **42** 491-500

Henry W H and Garrett C 1960 The Canadian standard free-air chamber for medium quality x-rays *Can. J. Phys.* **38** 1677-1689

Hobeila F and Seuntjens J 2002 Implementation of NIST XCOM-based photoelectric cross-sections in EGSnrc (abstract) *Med. Phys.* **29** 1353

Horowitz A and Horowitz Y S 1990 Optimisation of LiF:Cu,Mg,P for radiation protection dosimetry *Radiat. Prot. Dosim.* **33** 267-270

Horowitz A and Horowitz Y S 1992 Elimination of the residual signal in LiF:Cu,Mg,P *Radiat. Prot. Dosim.* **40** 265-267

Horowitz Y S, Moscovitch M and Dubi A 1983 Modified general cavity theory applied to the calculation of gamma dose in ^{60}Co thermoluminescence dosimetry *Phys. Med. Biol.* **28** 829-840

Horowitz Y S 1984a *Thermoluminescence and Thermoluminescent Dosimetry, Volume I* (Boca Raton, FL: CRC Press)

Horowitz Y S 1984b *Thermoluminescence and Thermoluminescent Dosimetry, Volume II* (Boca Raton, FL: CRC Press)

Horowitz Y S and Horowitz A 1990 Characterisation of LiF:Cu,Mg,P (GR-200) for personnel thermoluminescence dosimetry *Radiat. Prot. Dosim.* **33** 279-282

Horowitz Y S 1993 LiF:Mg,Ti versus LiF:Mg,Cu,P: the competition heats up *Radiat. Prot. Dosim.* **47** 135-141

Horowitz Y S, Avila O and Rodriguez-Villafuerte M 2001 Theory of heavy charged particle response (efficiency and supralinearity) in TL materials *Nucl. Instrum. Methods* B **184** 85-112

Horowitz Y S 2001 Theory of thermoluminescence gamma dose response: the unified interaction model *Nucl. Instrum. Methods* B **184** 68-84

Hubbell J H and Seltzer S M 1997 *Tables of X-Ray Mass Attenuation Coefficients and Mass Energy-Absorption Coefficients* (version 1.03) http://physics.nist.gov/xaamdi (Gaithersburg, MD: National Institute of Standards and Technology)

International Commission on Radiological Units and Measurements (ICRU) 1984 *Stopping Powers for Electrons and Positrons* ICRU Report 37

International Organization for Standardization (ISO) 1996 *X and gamma reference radiation for calibrating dosemeters and doserate meters and for determining their response as a function of photon energy - Part 1: Radiation characteristics and production methods* ISO Publication 4037-1

Janovský I and Ross C K 1993 *The IRS Thermoluminescent Dosimetry System* NRC Report PIRS-0369 (Ottawa, ON: National Research Council Canada)

Johns H E and Cunningham J R 1983 *The Physics of Radiology* 4th edn. (Springfield, IL: Thomas)

Kawrakow I 2000 Accurate condensed history Monte Carlo simulation of electron transport. I. EGSnrc, the new EGS4 version *Med. Phys.* **27** 485-498

Kawrakow I and Rogers D W O 2001 *The EGSnrc Code System: Monte Carlo Simulation of Electron and Photon Transport* NRC Report PIRS-701 (Ottawa, ON: National Research Council Canada)

Kearsley E 1984 A new general cavity theory *Phys. Med. Biol.* **29** 1179-1187

King J J and Cassata J R 2000 An inventory review of the Naval Dosimetry Center's DT-648 thermoluminescent dosimeter *Radiat. Prot. Manag.* **17** 17-22

Klemic G, Shobe J, Sengupta S, Shebell P, Miller K, Carolan P T, Holeman G, Kahnhauser H, Lamperti P, Soares C, Azziz N and Moscovitch M 1999 State of the art of environmental dosimetry: 11th international intercomparison and proposed performance tests *Radiat. Prot. Dosim.* **85** 201-206

McKeever S W S, Moscovitch M and Townsend P D 1995 *Thermoluminescence Dosimetry Materials: Properties and Uses* (Ashford: Nuclear Technology Publishing)

Mobit P N, Nahum A E and Mayles P 1997 An EGS4 Monte Carlo examination of general cavity theory *Phys. Med. Biol.* **42** 1319-1334

Moscovitch M 1999 Personnel dosimetry using LiF:Mg,Cu,P *Radiat. Prot. Dosim.* **85** 49-56

Nakajima T, Murayama Y, Matsuzawa T and Koyano A 1978 Development of a new highly sensitive LiF thermoluminescence dosimeter and its applications *Nucl. Instrum. Methods* **157** 155-162

Nelson W R, Hirayama H and Rogers D W O 1985 *The EGS4 Code System* SLAC-265 (Stanford, CA: Stanford Linear Accelerator Center)

Olko P and Booz J 1990 Photon induced microdosimetric distributions in nanometer and micrometer sites *Radiat. Prot. Dosim.* **31** 205-209

Olko P, Bilski P, Ryba E and Niewiadomski T 1993 Microdosimetric interpretation of the anomalous photon energy response of ultra-sensitive LiF:Mg,Cu,P TL dosemeters *Radiat. Prot. Dosim.* **47** 31-35

Olko P, Bilski P and Michalik V M 1994 Microdosimetric analysis of the response of LiF thermoluminescent detectors for radiations of different qualities *Radiat. Prot. Dosim.* **52** 405-408

Olko P 1996 Microdosimetric interpretation of thermoluminescence efficiency of LiF:Mg,Cu,P (MCP-N) detectors for weakly and densely ionising radiations *Radiat. Prot. Dosim.* **65** 151-158

Oster L, Horowitz Y S and Horowitz A 1996 Further studies of the stability of LiF:Mg,Cu,P (GR-200) at maximum readout temperatures between 240°C and 280°C *Radiat. Prot. Dosim.* **65** 159-162

Perry O R, Moscovitch M, Velbeck K J and Rotunda J E 1999 LiF:Mg,Cu,P based environmental dosemeter and dose calculation algorithm *Radiat. Prot. Dosim.* **85** 273-281

Pradhan A S and Bhatt R C 1989 Thermoluminescence response of LiF:Mg,Cu,P and LiF TLD-100 to thermal neutrons, ^{241}Am alphas and gamma rays *Radiat. Prot. Dosim.* **27** 185-188

Press W H, Teukolsky S A, Vetterling W T and Flannery B P 1992 *Numerical Recipes in FORTRAN: Second Edition* (Cambridge: Cambridge University Press)

Ranogajec-Komor M, Muhiy-Ed-Din F, Milkovic D and Vekic B 1993 Thermoluminescence characteristics of various detectors for x ray diagnostic measurements *Radiat. Prot. Dosim.* **47** 529-534

Rogers D W O and Kawrakow I 2000 *Distribution Area for EGSnrc: A Unix/Linux-based System for Monte Carlo Simulation of Electron and Photon Transport* http://www.irs.inms.nrc.ca/inms/irs/EGSnrc/EGSnrc.html

Rogers D W O, Faddegon B A, Ding G X, Ma C M, Wei J and Mackie T R 1995 BEAM: a Monte Carlo code to simulate radiotherapy treatment units *Med. Phys.* **22** 503-524

Rogers D W O, Kawrakow I, Seuntjens J P and Walters B R B 2001 *NRC User Codes for EGSnrc* NRC Report PIRS-702 (Ottawa, ON: National Research Council Canada)

Sáez-Vergara J C and Romero A M 1996 The influence of the heating system on the hypersensitive thermoluminescent material LiF:Mg,Cu,P (GR-200) *Radiat. Prot. Dosim.* **66** 431-436

Sáez-Vergara J C, Romero A M, Ginjaume M, Ortega X and Miralles H 1999 Photon energy response matrix for environmental monitoring systems based on LiF:Mg,Ti and hypersensitive phosphors (LiF:Mg,Cu,P and α-Al_2O_3:C) *Radiat. Prot. Dosim.* **85** 207-211

Seelentag W W, Panzer W, Drexler G, Platz L and Santner F 1979 *A Catalogue of Spectra Used for the Calibration of Dosemeters* GSF-Bericht 560 (München: Gesellschaft für Strahlen und Umweltforschung)

Shortt K R and Ross C K 1986 *The Canadian ^{60}Co Exposure Standard* NRC Report PIRS-0052 (Ottawa, ON: National Research Council Canada)

Shortt K R, Ross C K and Janovský I 1997 The response of LiF TLDs to ^{137}Cs and ^{60}Co γ rays *Radiat. Prot. Dosim.* **69** 257-266

Shoushan W, Guolong C, Fang W, Yuanfang L, Ziying Z and Jianhuan Z 1986 Newly developed highly sensitive LiF (Mg,Cu,P) TL chips with high signal-to-noise ratio *Radiat. Prot. Dosim.* **14** 223-227

Stewart R D, Wilson W E, McDonald J C and Strom D J 2002 Microdosimetric properties of ionizing electrons in water: a test of the PENELOPE code system *Phys. Med. Biol.* **47** 79-88

Storm E and Israel H I 1970 Photon cross sections from 1 keV to 100 MeV for elements Z=1 to Z=100 *Atomic Data and Nuclear Data Tables* **7** 565-681

Tochilin E, Goldstein N and Lyman J T 1968 The quality and LET dependence of three thermoluminescent dosimeters and their potential use as secondary standards *Proc. 2nd Int. Conf. on Luminescence Dosimetry (US AEC Conf. 680920)* (Springfield, VA: NTIS)

Turner J E, Hamm R N, Wright H A, Modolo J T and Sordi G M A A 1980 Monte Carlo calculation of initial energies of Compton electrons and photoelectrons in water irradiated by photons with energies up to 2 MeV *Health Phys.* **39** 49-55